Inter-fibre failure under biaxial loads in glass–epoxy composite materials: Effect of the presence of a nearby fibre

Carlos Sandino [*], Elena Correa , Federico París

Group of Elasticity and Strength of Materials, School of Engineering, Universidad de Sevilla, Camino de los Descubrimientos s/n, 41092 Seville, Spain

A R T I C L E   I N F O

A B S T R A C T

Fibre-reinforced composite materials are especially prone to transverse failure. It appears at the lamina level following the mechanism known as matrix/inter-fibre failure. This mechanism of damage is associated with the appearance of fibre–matrix debonds (interface cracks), as shown in previous numerical micromechanical studies. After the nucleation, growth and kinking into the matrix, these interface cracks give rise to the final macro-failure.

When compared to uniaxial loading, the growth stages of this mechanism of damage (analysed in light of Interfacial Fracture Mechanics) show some alterations under different combinations of biaxial loads. This work gives a step forward and focuses on the micromechanical BEM study of the evolution of an interface crack in the presence of a neighbouring fibre.

Thus, after considering a transverse tensile load (nominally responsible for the failure) a secondary transverse load is also applied (tensile or compressive, perpendicular to the primary load). When considering the two-fibre BEM model, the results obtained lead to identifying the neighbouring fibre locations that act as accelerative agents on failure progression and establishing the effect of the biaxial load on them. Specifically, when a secondary tensile load is applied, the presence of the nearby fibre (for most of its positions) confirms the slight inhibition of the mechanism of failure for biaxial tensile loads already referred to in previous single-fibre studies by the authors. As the secondary tensile load increases, it tends to mitigate the effect of the presence of the neighbouring fibre that was previously observed for uniaxial tensile load. The opposite effects are found when a secondary compressive load is considered, which intensifies the alterations of the presence of the neighbouring fibre on the interface crack growth. Experimental evidence on some aspects is provided confirming the associated conclusions derived from the numerical models.

1. Introduction

The study of the damage mechanism taking place in long fibre-reinforced composites at the micromechanical level is fundamental for the improvement of industrial applications involving these materials. In this regard, transverse failure, which starts with small interfacial debonds that lead to a transverse crack that produces the failure at the ply level, plays a key role. This failure is generated by the damage mechanism known as inter-fibre or matrix failure, which is due to loads perpendicular to the direction of the fibres in unidirectional laminates or impact loads in multidirectional laminates. The importance of this mechanism lies in the fact that it usually defines the damage initiation in any laminate.

At the micromechanical level, the inter-fibre failure has been numerically analysed under uniaxial tension [1,2] and under uniaxial compression [3–5], by means of BEM single-fibre models. In these studies, based on the hypothesis that transverse failure starts with the appearance of debonds at the interface between the fibres and the surrounding matrix, the different stages of the damage mechanism that lead to the macro-failure were identified. In the case of the initiation of the failure due to a transverse tensile load, three stages were considered, as shown in Fig. 1:

Stage 1. Crack nucleation: the initiation of the damage mechanism is assumed to be controlled by the radial stress at the interface. For a single-fibre case, the maximum value of the radial stress responsible for the failure is detected at 0° from the direction of the uniaxial tensile load, resulting in the appearance of the first debond.

Stage 2. Interface crack growth: starting from the initial debond, the
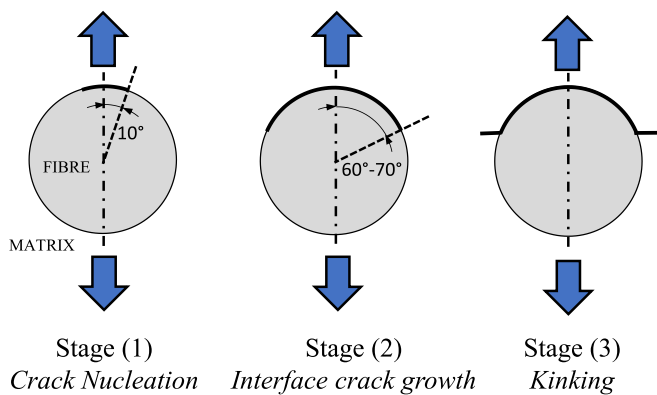

Fig. 1. Micromechanical phases of the inter-fibre failure identified with a single-fibre model under uniaxial tension.

crack grows unstably and symmetrically along the interface until it reaches a certain length (60°-70°) from the direction of the external load. The end of this stage coincides with the appearance of a finite contact zone at the crack tips.

Stage 3. Kinking: the crack growth becomes stable, which favours a change in the direction of propagation, the crack kinking into the matrix in the direction perpendicular to the tensile load applied. This crack continues growing through the matrix, where the coalescence of cracks leads to failure at the lamina level.

After the identification of the differentiated stages of the damage mechanism and the use of single-fibre models, some authors have included a greater number of fibres in their numerical tools (BEM or FEM). Such is the case of the studies presented in [6,7] for uniaxial tensile and compressive loads respectively. These works are focused on the BEM analysis of the interface crack growth in the presence of a nearby undamaged fibre. Thus, a two-fibre model is employed for analysing the influence of the presence of the nearby fibre and its position on the propagation of the crack. Multifibre FEM models are presented in [8], using cohesive elements, and in [9], applying Linear Elastic Interface Models (LEBIM).

The study of this damage mechanism has also been analysed from the point of view of Finite Fracture Mechanics. Such is the case of [10] for the tensile uniaxial case. In [11], the authors proposed a model based on Finite Fracture Mechanics for the study of the interface debonding under a combination of plane tension and out-of-plane shear.

Some other numerical studies have focused on the initial stage of the damage, such is the case of [12,13], whereas other authors have analysed the state previous to the appearance of the macro-crack [14,15]. In [16,17], different models of Representative Volume Elements have been implemented, in order to study the influence of the fibre volume fraction, the distance between interface cracks, the distance to the free surface or the distance to the 0°/90° interface in cross-ply laminates, on the evolution of the Energy Release Rate. All these approaches are especially appropriate for the study of fibre-reinforced composite laminates containing ultra-thin plies, in order to have a better understanding of the phenomenon known as the scale effect ([18–20]).

Regarding the experimental approaches of this problem, some authors have studied the damage mechanism at the micromechanical level. These studies included the outstanding works in the observation of interface cracks presented in [21] for static loads, and in [22] for dynamic loads. The presence of thermal residual stresses, which represent an important aspect to be considered in the curing process of fibrous composites, is evaluated in [23]. Other studies include the effects of the fibre type [24], high and low curing temperatures [25], the thickness of 90° plies in cross-ply laminates [26], or the use of X-ray micro-tomography in single-fibre specimens to analyse the initial debond and the propagation of the interface crack [27]. Recent approaches include the works presented in [28], which presents optical microscopy

measurements of the different stages of the damage mechanism under tension in cross-ply laminates, and in [29], which follows the same approach for the compressive damage mechanism.

With respect to the aforementioned stages of the damage mechanism, some authors have considered the possible alterations that biaxial transverse loading could cause. It has been historically assumed that, when considering biaxial transverse loads, inter-fibre failure occurs in a plane governed by the components of the stress vector associated with the referred plane [30]. This fact implies that, for instance, a secondary load transverse to a main tensile load would not be relevant in the generation of the interface crack. In order to confirm this hypothesis in the case of a single-fibre model under biaxial loads, the studies carried out in [31,32] analysed the possible effects of a secondary transverse load on the initiation and propagation of an interface crack governed by tensile or compressive loads.

In order to approach the problem from an experimental point of view, the design of cruciform composite specimens for biaxial testing was carried out in [33]. More specifically, four different designs of cruciform specimens consisting of 90° unidirectional composite laminates were proposed and studied for different load levels, using FEM models. This analysis was validated by the results of the study presented in [34], in which, the design of a biaxial device adapted for use in a universal uniaxial testing machine was carried out to perform experimental biaxial tests. Subsequently, based on the study presented in [33], the design and manufacture of cruciform specimens and the development of an experimental testing campaign were carried out in [35].

In the present study, the authors follow the approach of the two-fibre models presented in [6,7] for uniaxial tension and compression and the analysis of biaxial loading for a single-fibre case presented in [31,32]. To this aim, a two-fibre BEM model is used to observe the influence of a transverse (tensile or compressive) secondary load on the interface crack growth when a tensile main load is considered. Thus, the alterations produced by the presence of a neighbouring undamaged fibre are analysed by modifying the value of the secondary load and comparing the results with the uniaxial tensile case [6]. The analysis of all the cases under consideration is focused on the evolution of the Energy Release Rate during the interface crack growth and its use to predict some aspects such as the length and morphology of the crack. This work is structured as follows: Section 2 is devoted to the description of the BEM numerical model; in Section 3 the tension–tension biaxial cases (T-nT) are studied; and Section 4 corresponds to the tension–compression biaxial cases (T-nC); in Section 5, the most important results are summarised and discussed, and they are compared with experimental evidence. Finally, Section 6 is devoted to the main conclusions of this study.

2. Numerical model

In this work, the numerical study was carried out using a tool based on BEM [36] and developed in [37]. This BEM code allows the numerical analysis of plane elastic problems for contact and interface cracks to be performed. A scheme representing the model employed in this work is shown in Fig. 2. It represents the case of a crack that grows (under the plane strain hypothesis) along the interface between the matrix and the so-called primary fibre, in the presence of a secondary undamaged fibre. The appearance of the first debond is assumed to be associated with the direction of the primary tensile load for all cases under consideration, even though the secondary load and the position of the secondary fibre could alter its position. This assumption is reinforced by the results obtained in [35] where in all T-nT and T-nC cases the macro-failure always occurred perpendicular to the main external tension. In order to compare the results of this study with the biaxial single-fibre case [31] and the uniaxial two-fibre case [6], a symmetrical model is established. Thus, the presence of the secondary fibre produces the same effects at both crack tips. Notice that now the entire model consists of three fibres.

Solids 'M', 'PF' and 'SF' represent the matrix and the primary/secondary fibres respectively. The fibres' size is defined by the radius r_1
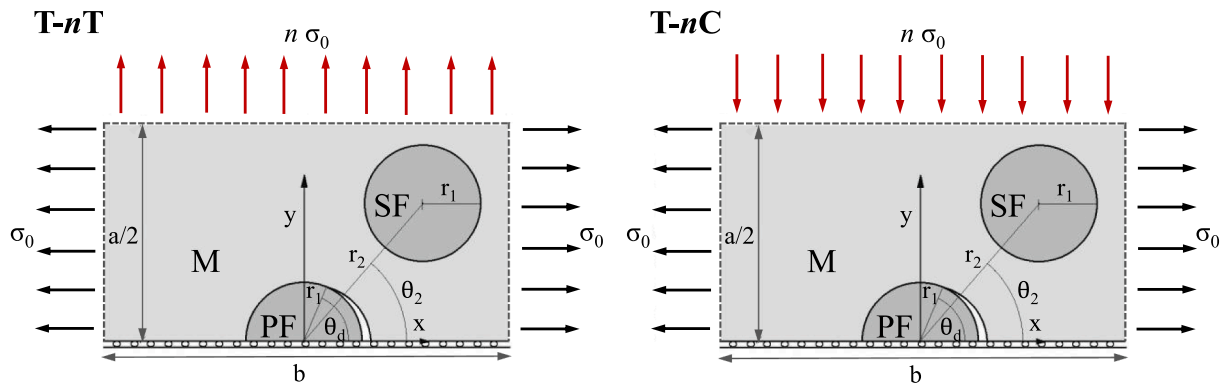
Fig. 2. Model including a primary fibre with an interface crack and an undamaged secondary fibre, under two different biaxial configurations.

(r_1=7.5·10^{-6}m) and the matrix is large enough in order to avoid the border effect (b=100·r_1 and a=b). The position of the secondary fibre is defined by parameters r_2 and θ_2 and is modified to analyse different relative positions between the fibres. For this study, the initial distance employed between the fibres is $r_2=r_2^0$=2.416·r_1, which corresponds to the distance calculated for a fibre volume fraction V_f=62% and hexagonal packing.

With regard to the loads applied, the different cases follow the notation T-nT/T-nC, where the first T represents the transverse tension nominally responsible for the failure (σ_0, aligned with the x-axis) and the term nT/nC corresponds to the secondary tensile or compressive load (aligned with the y-axis). This secondary load is a fraction of that applied on the x-axis, this fraction being defined by coefficient n. The n values considered in this study are n = 0, 0.25, 0.5, 0.75, 1.

The materials chosen for the analysis correspond to a glass fibre-epoxy matrix system. The elastic properties are included in Table 1.

To describe the problem from the Fracture Mechanics point of view, the Energy Release Rate, G, is used. It is calculated following Eq. (1) (based on [38]), for a circular crack that propagates from a certain debonding angle, θ_d, Fig. 2, to $\theta_d + \Delta\theta_d$ ($\Delta\theta_d \ll \theta_d$):

$$G(\theta_d, \Delta\theta_d) = \frac{1}{2\Delta\theta_d} \int_{\theta_d}^{\theta_d+\Delta\theta_d} [\sigma_{rr}(\theta_d + \theta)\Delta u_r(\theta_d - \Delta\theta_d + \theta)$$
$$+ \sigma_{r\theta}(\theta_d + \theta)\Delta u_\theta(\theta_d - \Delta\theta_d + \theta)]d\theta \tag{1}$$

where θ is the circumferential coordinate with reference to the x-axis. σ_{rr} and $\sigma_{r\theta}$ represent the radial and shear stresses along the interface, and Δu_r and Δu_θ represent the relative displacements of the crack faces. Modes of fracture I and II are obviously considered in Eq. (1), associated with σ_{rr} and $\sigma_{r\theta}$ respectively. For this study, the value of $\Delta\theta_d$ employed is 0.5°.

Dimensionless results for G will be presented. These values are obtained, following [39,40], by dividing the values of G by G_0:

$$G_0 = \frac{1 + \kappa^m}{8\mu^m}\sigma_0^2 r_1\pi \tag{2}$$

where $\kappa^m = 3-4\nu^m$ and μ^m is the shear modulus of the matrix.

Table 1
Elastic properties of the bi-material system.

Material	Young modulus, E (Pa)	Poisson coefficient, ν
Matrix (epoxy)	$E^m = 2.79 \cdot 10^9$	$\nu^m = 0.33$
Fibre (glass)	$E^f = 7.08 \cdot 10^{10}$	$\nu^f = 0.22$

3. T-nT Cases

3.1. Energy Release Rate

In this Section, the Energy Release Rate, G, is calculated from Eq. (1) for a growing interface crack. This allows the problem to be characterised from the Interface Fracture Mechanics point of view. Considering the model presented in Fig. 2, the damage was assumed to appear as an initial debond of θ_d=10° [6,31]. Then, G was obtained for a debonding interval 10°≤θ_d≤150°, using the single-fibre model (reference case) and the two-fibre model (with different relative positions between the fibres), and applying the biaxial tensile cases T-nT. Regarding the two-fibre case, for any biaxial loading configuration and any relative angle between the fibres θ_2, the appearance of the initial debond follows the same tendency of the single-fibre case, even though the alterations of the radial stress along the undamaged fibre–matrix interface could modify the position of the initial debond. However, the experimental evidence presented in [35] (for biaxial T-nT and T-nC cases) reveals that, regardless of the position of the initial debond and the propagation of the interface crack, the latter stages of the mechanism of damage and the final macro-crack are contained in the failure plane perpendicular to the main tensile load. This evidence implies that the main external tension is responsible for the failure and suggests that the location of the initial debond would in any case lead to the interfacial growth assumed here. Therefore, for all the cases considered in this study, the position of the initial debond is the same, in order to obtain a better understanding of the effects of a growing secondary transverse load.

The evolution of G calculated with the single-fibre model is represented in Fig. 3. These results obviously coincide with those obtained in [31] and were employed as a reference for the two-fibre cases. As can be observed, for T-0.25 T and T-0.5 T (Fig. 3a), the global G level slightly decreases with respect to the uniaxial case (T-0), whereas for T-0.75 T and T-T (Fig. 3b), it tends to recover the G level of T-0.

Regarding the qualitative point of view, propagation under Mode I becomes more relevant as the secondary load increases: the G_I level rises above the uniaxial case and the mixed mode propagation ends at larger debonds, which translates the G maxima for T-0.75 T and T-T to higher values of θ_d. Thus, Mode I is still active for larger debonds because the secondary transverse load is approximately aligned with the zones where the contact zone was supposed to grow for the uniaxial case [1,6], which produces an inhibition of the contact and pure Mode II propagation as the secondary load increases.

However, the G value associated with the first debond considered ($G_{\theta_d=10°}$), which is mostly associated with Mode I propagation, slightly decreases as the secondary load increases, as shown in Fig. 4. This fact could be related to the level of load needed to initiate the propagation, as explained in previous studies [6,31]. Thus, when compared to the uniaxial case, the growth of the incipient crack would require a higher level of external load to be applied. Therefore, increasing values of the
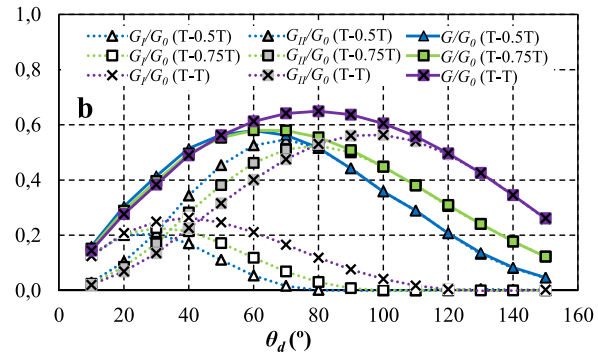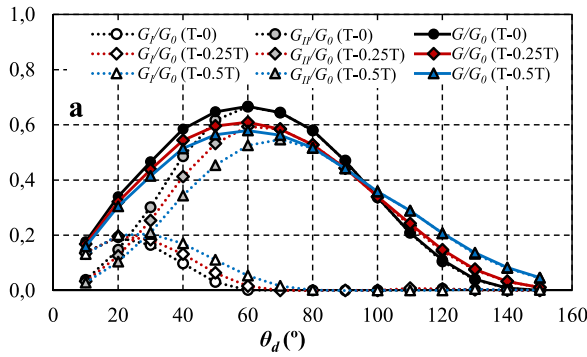
Fig. 3. G/G_0, G_I/G_0 and G_{II}/G_0 versus θ_d (single-fibre case), for T-nT: a) $n = 0, 0.25, 0.5$; b) $n = 0.5, 0.75, 1$.
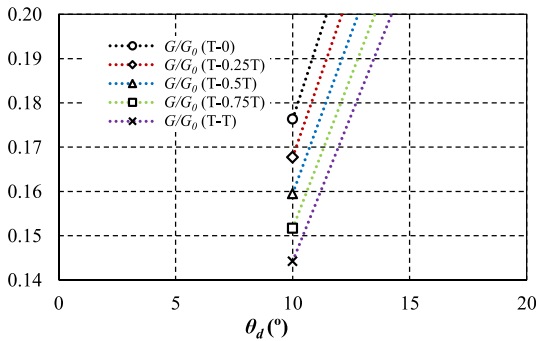

Fig. 4. Detail of G/G_0 versus θ_d (single-fibre case) for T-nT ($n = 0, 0.25, 0.5, 0.75, 1$).

secondary tensile load involve a slight inhibition of the mechanism of damage, representing a protective effect versus failure with respect to the uniaxial case.

Another interesting analysis regarding the effect of the biaxial tensile load versus failure can be carried out if the maximum value of the Energy Release Rate (G_{max}) is now selected as a representative parameter with respect to the inhibition or promotion of failure, as commented in [41]. In view of the results represented in Fig. 3, and taking the uniaxial case as a reference, the biaxial loading cases tend to inhibit the propagation of the interface crack, as the value of G_{max} for these cases is smaller than the reference case. Thus, the cases T-0 and T-T would be the most prone to failure, whereas the cases T-0.5 T and T-0.75 T would be the less likely to cause crack propagation.

Once the single-fibre case was analysed, the same approach was implemented for the two-fibre model. The evolution of G during the propagation ($10°\leq\theta_d\leq150°$) is calculated for the biaxial tensile cases T-nT. The propagation occurs in the presence of the undamaged secondary fibre for a fixed value of the distance between the centres of the fibres ($r_2=r_2^0$) and a range of relative angles ($25°\leq\theta_2\leq155°$). In Fig. 5, these results are plotted for a selection of θ_2 values ($\theta_2 = 25°, 40°, 60°, 90°, 120°, 155°$).

The G evolution of the interface crack for the angles $\theta_2=25°$ and $\theta_2=155°$ (fibres approximately aligned with the primary load) are represented in Fig. 5a and 5f. For these values of θ_2, the same tendency is observed for increasing values of the secondary tensile load, in particular, the global G level decreases until $\theta_d\approx80°$-$100°$ and increases for larger debonding angles. Nevertheless, for $\theta_2=40°$ (Fig. 5b), the biaxial load does not considerably alter the evolution of G, except for the increase produced for large debonding angles as the secondary tension increases.

Regarding the intermediate positions, they follow a different tendency. As shown in Fig. 5c, 5d and 5e for $\theta_2=60°$, $\theta_2=90°$ and $\theta_2=120°$, the global G level remains almost unaltered for $n = 0.25, 0.5$ with respect to the uniaxial case and increases considerably for $n = 0.75, 1$. It

is important to remark the displacement of the position of the maximum value of G for $\theta_2=90°$ ($\theta_d=100°$), which is related to the fact that the relative position of the fibres is aligned with the secondary load. This tends to amplify the radial displacement of the crack and, consequently, the disappearance of Mode I is reached at greater debonding angles than those of the single-fibre case, as observed in [6,7] (this fact will be further discussed).

Another interesting analysis is the comparison between the results of the two-fibre model for each biaxial case T-nT and the corresponding results of the single-fibre model. Considering the angles $\theta_2 = 25°, 40°, 60°, 90°, 120°, 155°$, this analysis is shown for the cases $n = 0, 0.25, 0.5$, and $n = 0.5, 0.75, 1$ in Figs. 6 and 7, respectively.

In general, in view of the results for a given value of θ_2, as the secondary load increases, G evolutions for all positions of the secondary fibre tend to approach the G level of its corresponding single-fibre case, which becomes more relevant when $n\geq0.5$ (Fig. 7). This effect means that the biaxial tensile load inhibits the alterations brought about by the secondary fibre, as the differences between all θ_2 cases among themselves and with respect to the single-fibre case become less pronounced for increasing values of the secondary load. In other words, as n increases, the evolution of G for all the θ_2 cases under consideration tends to converge toward the corresponding single-fibre case.

When Figs. 6 and 7 are analysed in more detail, it is worth highlighting that for the range $40°\leq\theta_2\leq90°$, (e.g. $\theta_2=60°$, Fig. 6c and 7c) and increasing values of the secondary load, the evolution of G tends to match the single-fibre case for large debonding angles ($\theta_d>90°$). On the contrary, for the range $90°\leq\theta_2\leq140°$, the evolution of G matches the single-fibre case for small debonding angles (e.g. $\theta_2=120°$, Fig. 6e and 7e).

It is also interesting to evaluate the effect of the secondary fibre for the same biaxial configuration. Considering the coefficient $n=0.5$, Fig. 8 shows the evolution of G, G_I and G_{II}, calculated with the two-fibre model for a selection of θ_2 values, also including the single-fibre curves associated with the cases T-0 and T-0.5 T.

When the two fibres are approximately aligned with the primary load ($25°\leq\theta_2\leq40°$ and $140°\leq\theta_2\leq155°$), the evolution of G is totally or partially above the single-fibre case. For the rest of the positions, G reaches lower values than those of the single-fibre case. This issue was also observed and explained in [6] for uniaxial tension, but the differences between the G evolutions with reference to the single-fibre case are less remarkable for the T-0.5 T case.

Regarding Mode I propagation, for $25°\leq\theta_2\leq50°$ G_I evolutions present significant differences with respect to the single-fibre case, both in the level of the curves and the position of their maxima, which tends to occur for $\theta_d\approx\theta_2$. This fact is produced by an increase in the radial displacement as the fibres tend to be aligned [6,7]. For $50°\leq\theta_2\leq120°$, G_I remains below the single-fibre case evolution, whereas for $130°\leq\theta_2\leq155°$ G_I stays above. The presence of the secondary fibre also affects the disappearance of G_I. For $40°\leq\theta_2\leq60°$, it occurs at larger debonding angles than in the biaxial single-fibre case, with all G_I

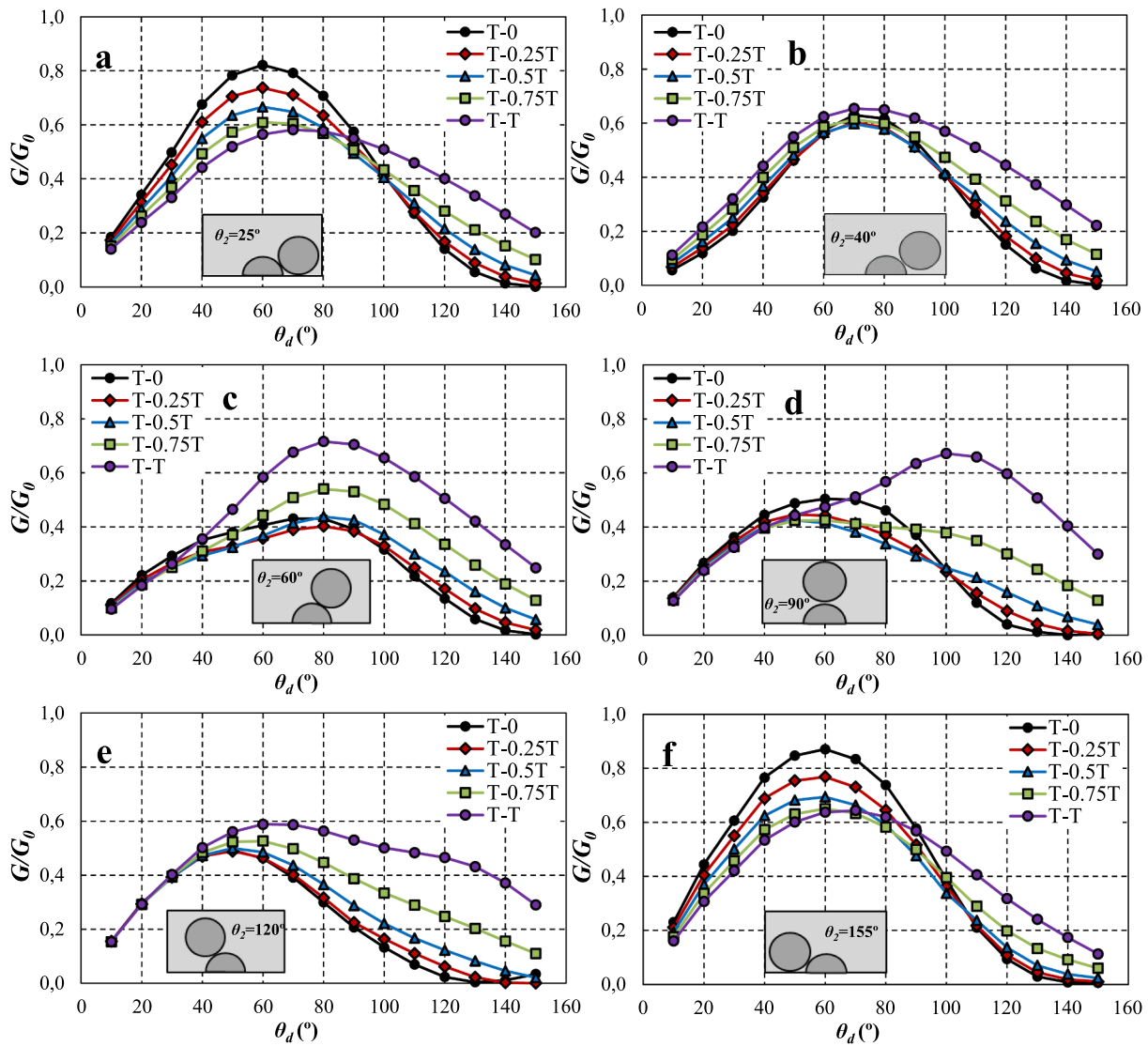**Fig. 5.** G/G_0 versus θ_d for T-nT ($n = 0, 0.25, 0.5, 0.75, 1$): a) $\theta_2 = 25°$, b) $\theta_2 = 40°$, c) $\theta_2 = 60°$, d) $\theta_2 = 90°$, e) $\theta_2 = 120°$, f) $\theta_2 = 155°$.

evolutions vanishing for higher θ_d values than in the uniaxial single-fibre case.

With reference to the G_{II} distributions, the maximum is reached at $\theta_d = 70°$ for the single-fibre case. Nevertheless, for $40° \leq \theta_2 \leq 70°$, the maximum takes place at a larger θ_d value than the single-fibre case and for $80° \leq \theta_2 \leq 140°$ the maximum occurs at a smaller θ_d value.

The results represented in Fig. 9 for the evolution of G for the case T-T and a selection of θ_2 values confirm the previously commented tendencies. As the value of the secondary load increases (in view of Figs. 8 and 9), and with respect to the uniaxial case [6], the differences between the evolution of G for the two-fibre cases and their corresponding single-fibre case become smaller. For T-T, these differences are more relevant for $60° \leq \theta_2 \leq 90°$, due to the fact that the disappearance of Mode I is produced for larger debonding angles (radial displacements increase as the fibres tend to be aligned with the secondary load), as well as the G_{II} maximum.

The analysis of the G value associated with the first debond considered ($G_{\theta_d = 10°}$) was also carried out for the two-fibre and biaxial loading cases. Fig. 10 represents the variation of $G_{\theta_d = 10°}$ for the two-fibre cases with respect to the single-fibre case. It is observed that, as could be expected from Fig. 4, when the secondary load was taken into consideration, $G_{\theta_d = 10°}$ is lower than the single-fibre uniaxial case value for most of the positions of the secondary fibre in the T-0.5 T case. For T-T,

this fact occurs for any position of the secondary fibre, confirming the inhibition of the mechanism of failure provoked by the biaxial loading, previously commented in this section. The location of the most protective effect produced by the secondary fibre is also modified as n increases: it was found at $\theta_2 = 60°$ for T-T, whereas for $n = 0, 0.5$, it was located at $\theta_2 = 40°$.

If the results of the two-fibre and single-fibre cases for each T-nT case are compared, taking the corresponding single-fibre case as a reference, $G_{\theta_d = 10°}$ is above the single-fibre case for a wider range of θ_2 values as the secondary load increases. However, the variations of $G_{\theta_d = 10°}$ with respect to the corresponding single-fibre case become smaller, confirming the hypothesis that the secondary tensile load reduces the influence of the secondary fibre on the interface crack growth.

In order to quantify these effects on failure, in [31] the authors explained the relation between the parameters from Interfacial Fracture Mechanics stress and energetic approaches for a small debond that grows in pure Mode I. More specifically, it was confirmed that the ratio between the uniaxial case and the biaxial cases for the maximum value of the radial stress along the interface $\left(\frac{\sigma_{rr}^{max}(T-0)}{\sigma_{rr}^{max}(T-nT)}\right)$ and for the square root of the G value associated with the first debond considered $\left(\sqrt{\frac{G_{\theta_d = 10°}(T-0)}{G_{\theta_d = 10°}(T-nT)}}\right)$ were equivalent. Thus, $\sqrt{\frac{G_{\theta_d = 10°}(T-0)}{G_{\theta_d = 10°}(T-nT)}}$ can be used as an

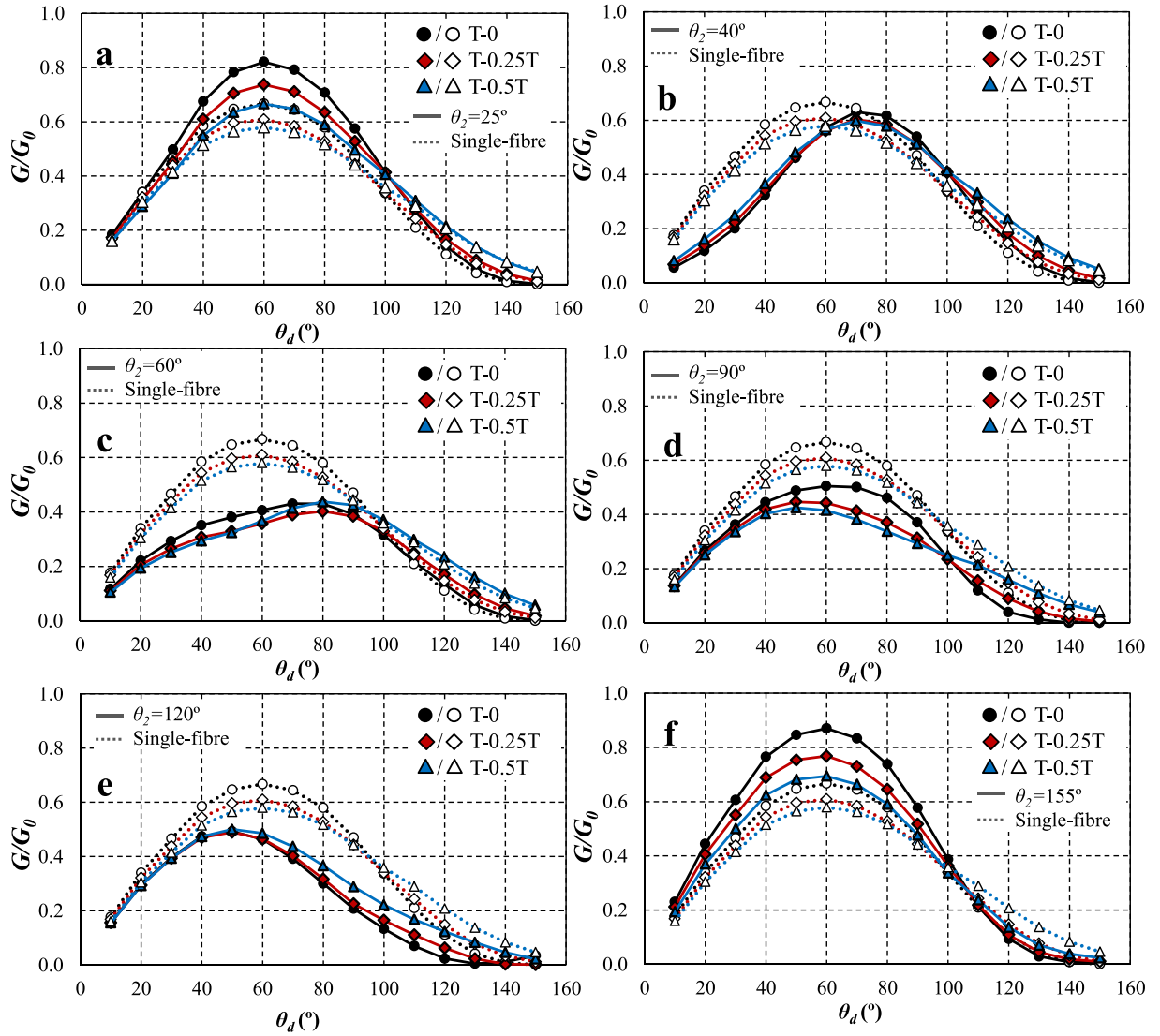**Fig. 6.** Comparison of G/G_0 versus θ_d for T-nT ($n = 0, 0.25, 0.5$), with reference to the single-fibre model: a) $\theta_2 = 25°$, b) $\theta_2 = 40°$, c) $\theta_2 = 60°$, d) $\theta_2 = 90°$, e) $\theta_2 = 120°$, f) $\theta_2 = 155°$.

indicator of the increase in the load that has to be applied to initiate the propagation of the interface crack. In the case of the single-fibre model, the results found (see Table 2) confirm a very close agreement with those obtained in [31] for $\theta_d=5°$, for all the T-nT cases considered.

This ratio can be modified for the two-fibre cases, which results in an interesting way to quantify the inhibition or promotion of the failure produced by the secondary fibre. Thus, the ratio $\sqrt{\frac{G_{\theta_d=10°}\ (\text{T-0, SF})}{G_{\theta_d=10°}\ (\text{T-}n\text{T})}}$ is proposed as an indicator of the effects produced by the presence of the secondary fibre. It is necessary to point out that, the reference value $G_{\theta_d=10°}$ corresponds to the uniaxial single-fibre case. Table 2 represents the values of this ratio for all θ_2 values and the T-nT cases. The results highlight that, as the secondary load increases, the differences in the increase of needed load to initiate the propagation become smaller and the accelerative effect (initially found for some θ_2 values) of the presence of the secondary fibre against failure $\left(\sqrt{\frac{G_{\theta_d=10°}\ (\text{T-0, SF})}{G_{\theta_d=10°}\ (\text{T-}n\text{T})}} < 1\right)$ tends to disappear.

3.2. Propagation of the interface crack

The end of the unstable crack growth can be predicted as explained

in [31], using the estimation of the critical value of the Energy Release Rate, G_c, based on [42], and comparing it with the corresponding G evolution:

$$G_c(\psi_k) = G_{1c}\left[1 + \tan^2[(1-\lambda)\psi_k]\right] \qquad (3)$$

where G_{1c} is the critical value of G_c for Mode I and λ is the fracture mode sensitivity parameter (in this study, $\lambda=0.25$, a typical value for the bi-material system under consideration). ψ_k is the local phase angle and represents the evolution of the fracture mode mixity. When the finite contact zone at the crack tip is developed and Mode I disappears, $\psi_k = 90°$ is reached. ψ_k can be calculated following [43]:

$$\psi_k(G) = 0.5\arccos\left[F(\varepsilon)^{-1}\frac{G_I - G_{II}}{G_I + G_{II}}\right] \qquad (4)$$

where $F(\varepsilon) = 1 + \left(\frac{\pi^2}{3} - 2\right)\varepsilon^2 + O(\varepsilon^4)$ and ε is the oscillatory index defined as:

$$\varepsilon = \frac{1}{2\pi}\ln\frac{1-\beta}{1+\beta} \qquad (5)$$

β being Dundurs parameter [44]. For the bi-material system under consideration $\varepsilon = -0.074$ and $F(\varepsilon)^{-1} = 1.0071$.
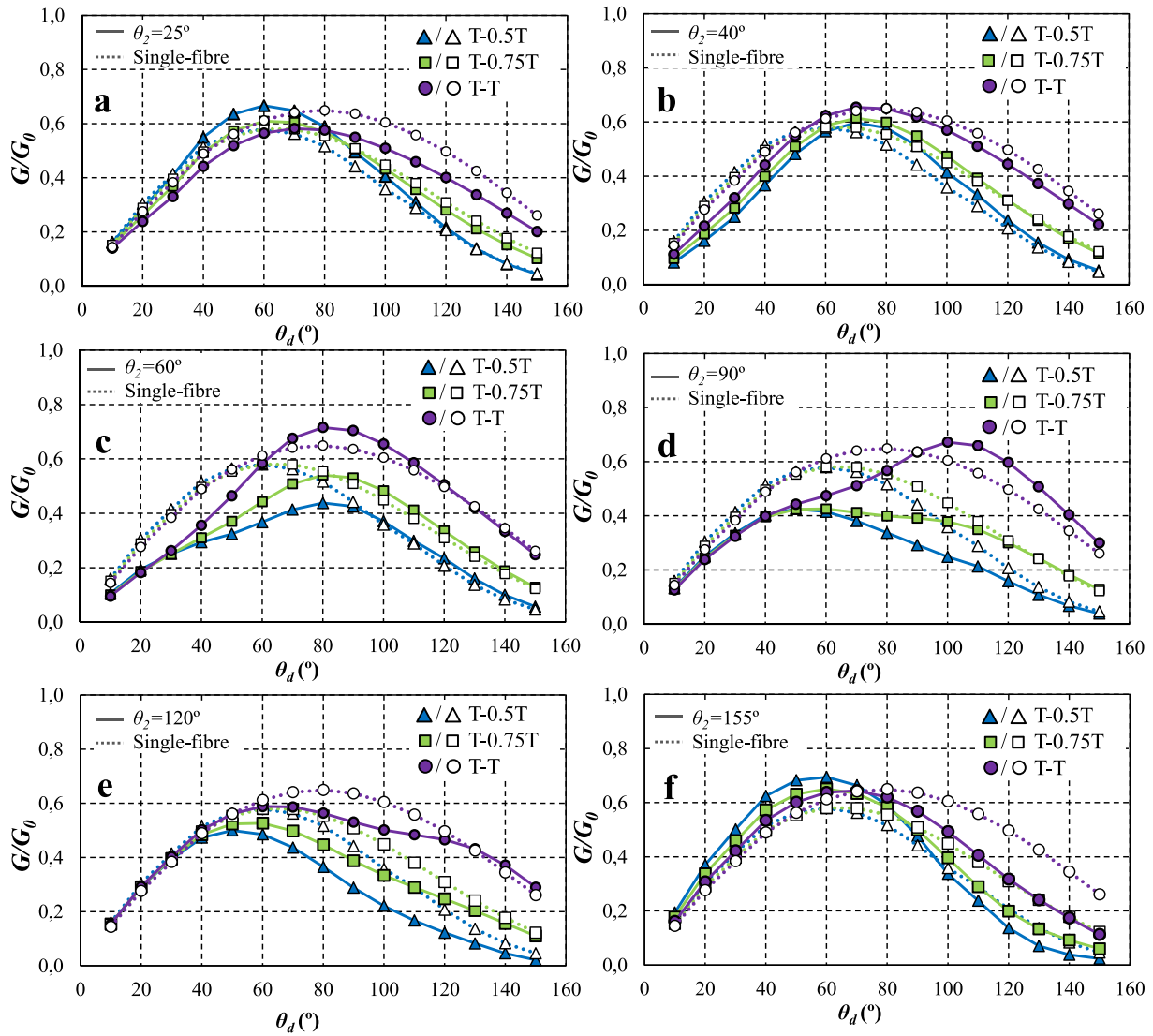
Fig. 7. Comparison of G/G_0 versus θ_d for T-nT ($n = 0.5, 0.75, 1$), with reference to the single-fibre model: a) $\theta_2 = 25°$, b) $\theta_2 = 40°$, c) $\theta_2 = 60°$, d) $\theta_2 = 90°$, e) $\theta_2 = 120°$, f) $\theta_2 = 155°$.

In the absence of direct experimental data, G_{1c} has been adjusted as detailed in [31], making the G_c value associated with the first debond considered coincide with the initial G value and establishing the uniaxial single-fibre G_{1c} value as the reference for all the cases under consideration. Thus, all G evolutions start at the same value, and therefore, a different level of load is needed to initiate the propagation for each case.

The comparison between G and G_c is shown in Fig. 11 for the single-fibre case and the biaxial tensile loads T-nT, with $n = 0, 0.25, 0.5$. The $n \geq 0.5$ cases are not included in Fig. 11 for the sake of clarity and simplicity, these cases following the same tendency shown in the figure. The crack length obtained for the end of the unstable growth is determined from the comparison between G and G_c at $\theta_d \approx 55°$ for T-0, $\theta_d \approx 60°$ for T-0.25 T and $\theta_d \approx 70°$ for T-0.5 T, coinciding with the appearance of a finite size contact zone at the crack tip. Therefore, the results obviously confirm the tendency observed in [31]: for increasing values of the secondary tensile load the interface crack reaches greater lengths of unstable growth.

The same approach was applied to the two-fibre cases. As a summary of the results of the prediction of the interface crack growth, a scheme representing the crack length at the end of the unstable growth is plotted in Fig. 12. This figure includes the single-fibre case and a selection of two-fibre cases, for all the biaxial T-nT loads ($n = 0, 0.25, 0.5, 0.75, 1$).

For $n = 0, 0.25$ and the range $25° \leq \theta_2 \leq 50°$, the crack reaches larger lengths of unstable growth than the single-fibre case. For $n=0.5$, this range of larger lengths is $25° \leq \theta_2 \leq 60°$. As the level of the secondary load increases, this θ_2 range becomes wider, it being $40° \leq \theta_2 \leq 100°$ for $n=0.75$ and $50° \leq \theta_2 \leq 120°$ for $n=1$. On the contrary, the positions where the lengths of unstable growth are smaller than in the single-fibre case are $60° \leq \theta_2 \leq 90°$ for $n=0$, $60° \leq \theta_2 \leq 80°$ for $n=0.25$, $80° \leq \theta_2 \leq 90°$ for $n=0.5$, $\theta_2=130°$ and $150° \leq \theta_2 \leq 155°$ for $n=0.75$ and $25° \leq \theta_2 \leq 30°$ and $140° \leq \theta_2 \leq 155°$ (positions aligned with the primary load) for $n=1$. Moreover, the end of the unstable growth is associated with the appearance of a finite size contact zone at the crack tip (or even before the appearance of the contact zone), except for the cases $30° \leq \theta_2 \leq 50°$ ($n = 0, 0.25$), since the crack stops growing after a considerable length of contact zone has been achieved.

It can also be observed in Fig. 12 that, for increasing values of the secondary load, the lengths of the debonding angles for the end of the unstable growth are larger, but there are fewer differences between all θ_2 cases and the single-fibre results. This fact suggests that, as mentioned in Section 3.1 in relation to the G evolutions of the two-fibre and single-fibre cases, when the secondary load increases, the effects produced by the biaxial load tend to mitigate the effects of the presence of the secondary fibre.
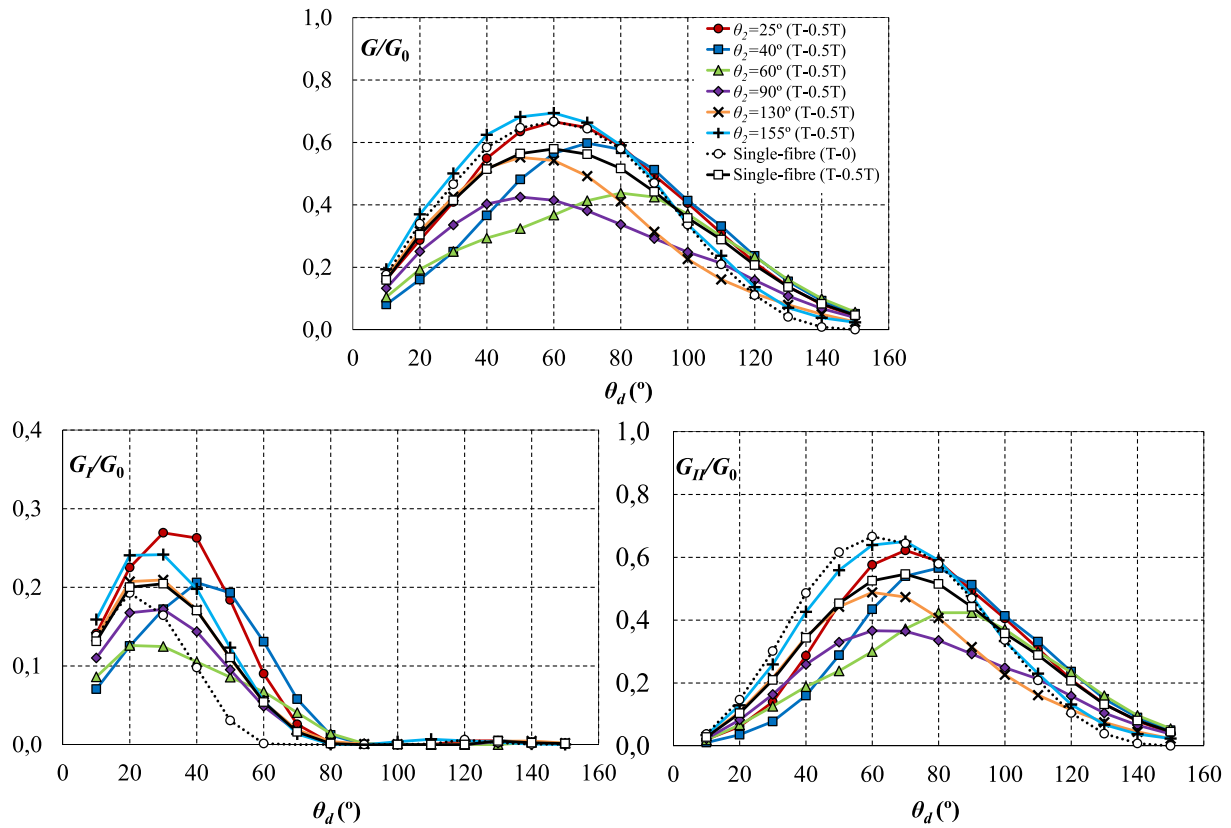
Fig. 8. G/G_0, G_I/G_0 and G_{II}/G_0 versus θ_d for T-0.5 T and $\theta_2 = 25°$, $40°$, $60°$, $90°$, $130°$, $155°$.
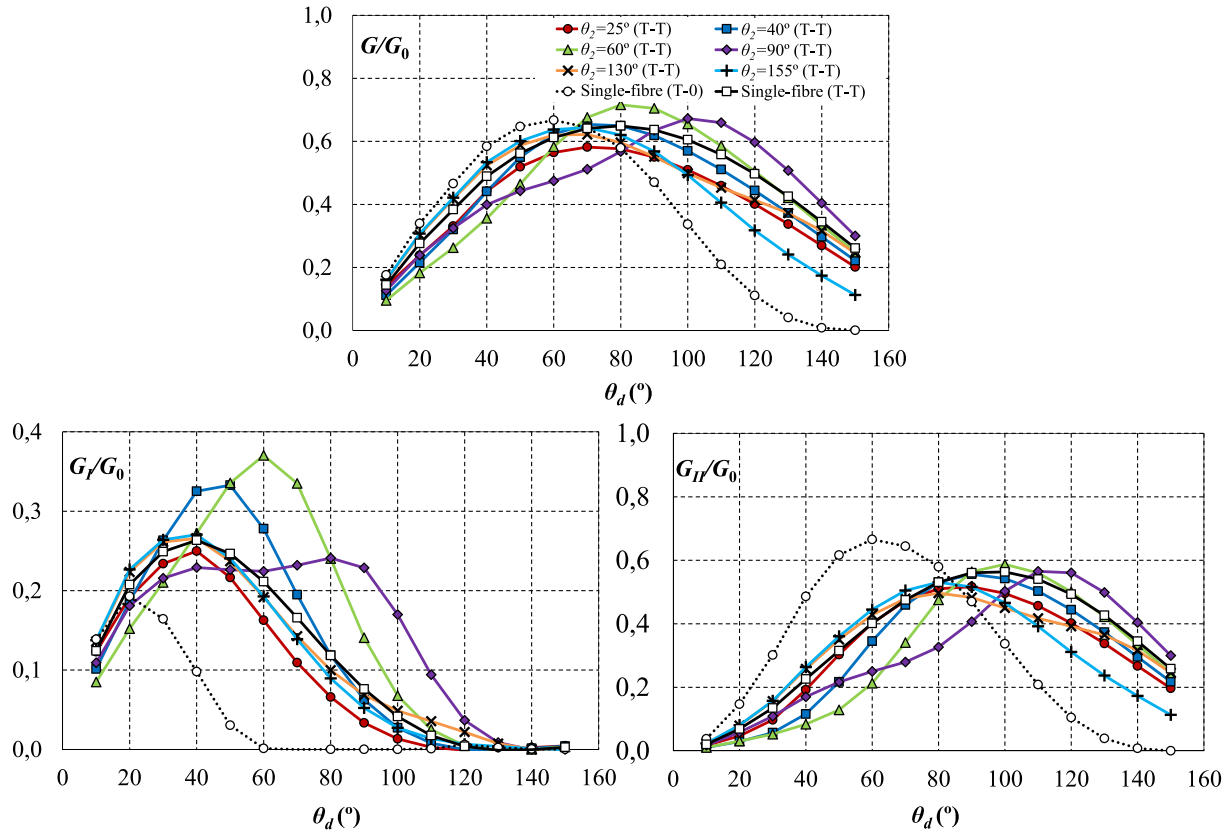
Fig. 9. G/G_0, G_I/G_0 and G_{II}/G_0 versus θ_d for T-T and $\theta_2 = 25°$, $40°$, $60°$, $90°$, $130°$, $155°$.
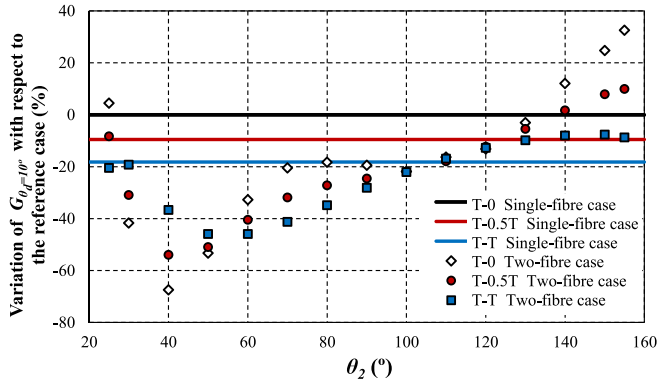
Fig. 10. Variation of $G_{\theta_d=10°}$ for the two-fibre cases with respect to the single-fibre case (T-nT, n = 0, 0.5, 1).

Table 2

$\sqrt{\dfrac{G_{\theta_d=10°}\ (T-0,\ SF)}{G_{\theta_d=10°}\ (T-nT)}}$ for the T-nT cases and the single-fibre (SF) and two-fibre (TF) models.

Case	SF	TF $\theta_2 = 25°$	TF $\theta_2 = 30°$	TF $\theta_2 = 40°$
T-0	1.000	0.975	1.307	1.770
T-0.25 T	1.024	1.009	1.254	1.609
T-0.5 T	1.050	1.042	1.201	1.472
T-0.75 T	1.077	1.079	1.155	1.356
T-T	1.105	1.121	1.113	1.254

Case	TF $\theta_2 = 50°$	TF $\theta_2 = 60°$	TF $\theta_2 = 70°$	TF $\theta_2 = 80°$
T-0	1.483	1.226	1.125	1.106
T-0.25 T	1.456	1.259	1.168	1.138
T-0.5 T	1.426	1.295	1.211	1.173
T-0.75 T	1.394	1.327	1.254	1.206
T-T	1.358	1.358	1.301	1.237

Case	TF $\theta_2 = 90°$	TF $\theta_2 = 100°$	TF $\theta_2 = 110°$	TF $\theta_2 = 120°$
T-0	1.121	1.127	1.109	1.062
T-0.25 T	1.133	1.129	1.106	1.065
T-0.5 T	1.150	1.131	1.102	1.067
T-0.75 T	1.164	1.131	1.098	1.068
T-T	1.177	1.132	1.094	1.070

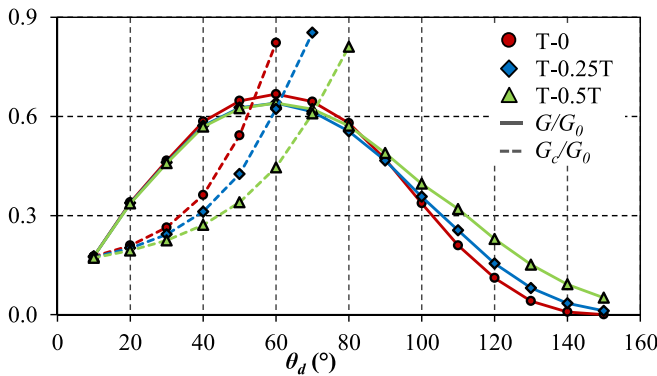| Case	TF $\theta_2 = 130°$	TF $\theta_2 = 140°$	TF $\theta_2 = 150°$	TF $\theta_2 = 155°$
T-0	1.003	0.943	0.892	0.875
T-0.25 T	1.015	0.968	0.927	0.911
T-0.5 T	1.027	0.992	0.962	0.952
T-0.75 T	1.039	1.015	1.000	0.997
T-T	1.052	1.042	1.039	1.046

Fig. 11. G/G_0 and G_c/G_0 versus θ_d for the single-fibre case and T-nT (n = 0, 0.25, 0.5).
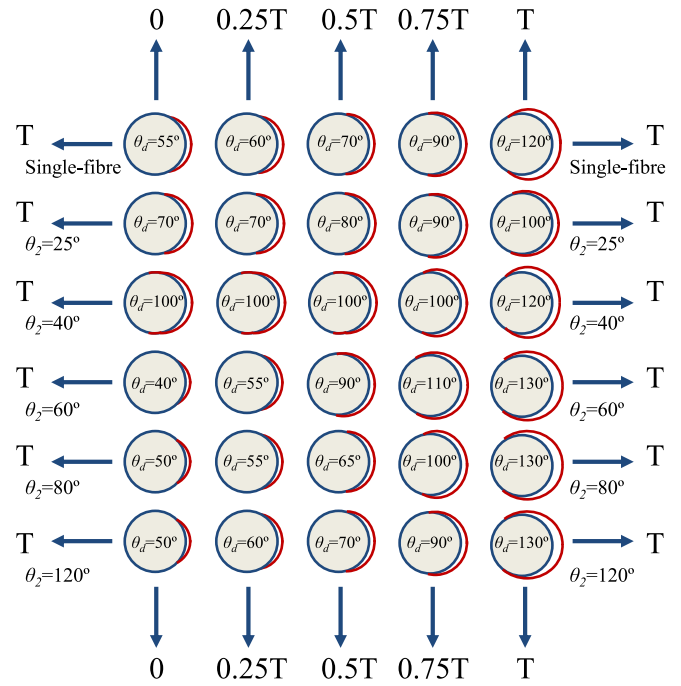

Fig. 12. Scheme of the crack length at the end of the unstable growth (T-nT).

4. T-nC Cases

4.1. Energy Release Rate

The same approach explained in the previous section was employed for the cases T-nC, i.e. tensile load T responsible for the failure and a secondary transverse compressive load, whose value is determined by factor n (n = 0, 0.25, 0.5, 0.75, 1). Thus, the Energy Release Rate, G, is calculated from Eq. (1) for a growing interface crack, considering an initial debond θ_d=10° (which appears aligned with the direction of the tensile load) and a debonding interval 10°≤θ_d≤150°.

The evolution of G for the single-fibre case is represented in Fig. 13. The results obviously agree with those presented in [31]. Contrary to the results represented in Fig. 3 for the T-nT cases, the effects of the compressive secondary load follow the same tendency for all the values of factor n: the values of G increase as the secondary load increases, especially within the range 40°≤θ_d≤100°, with no remarkable alterations from a qualitative point of view. This increase in the Energy Release Rate affects the values of $G_{\theta_d=10°}$ and G_{max}, selected as representative parameters of the effect of the secondary load on the inhibition or promotion of failure (as mentioned in Section 3.1). Thus, the presence of the secondary compressive load always represents an accelerative effect on the propagation of the interface crack, as expected in view of the results presented in [31].

This increase in the evolution of G is mainly due to the increase in G_{II}, as the compressive secondary load does not alter considerably the level of G_I. Moreover, the range of the propagation under mixed mode is slightly shortened by the secondary load: the disappearance of Mode I propagation occurs at θ_d=60° for T-0 and at θ_d=50° for T-C.

When including a secondary fibre in the model, the tendency on the G evolution is the same. The level of G increases as the secondary load increases, as can be observed in Fig. 14 for all the relative positions between the fibres represented (θ_2 = 25°, 40°, 60°, 90°, 120°, 155°). This is especially relevant for θ_2 = 25°, 155° (fibres aligned with the tensile load), θ_2=90° (fibres aligned with the compressive load) and θ_2=60° (intermediate position of the secondary fibre, in front of the crack growth range). The secondary load affects to a lesser extent other positions like θ_2=40° or θ_2=120° (intermediate position, further from the
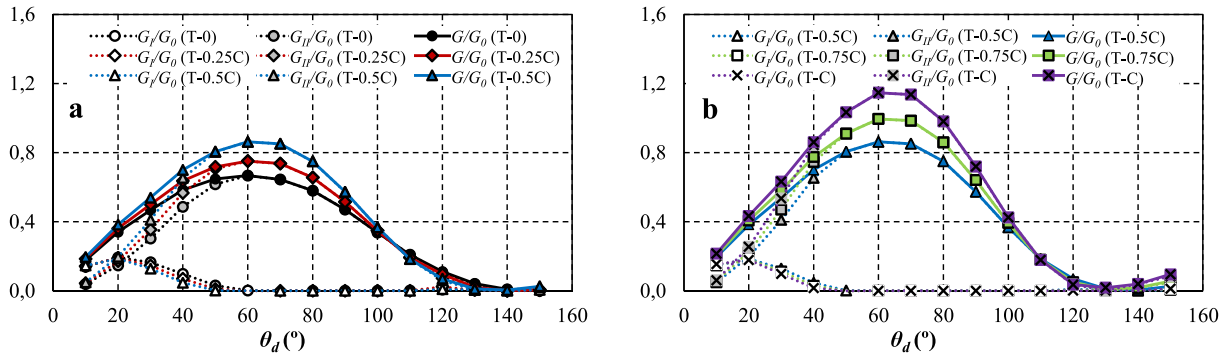
Fig. 13. G/G_0, G_I/G_0 and G_{II}/G_0 versus θ_d (single-fibre case), for T-nC: a) $n = 0$, 0.25, 0.5; b) $n = 0.5$, 0.75, 1.
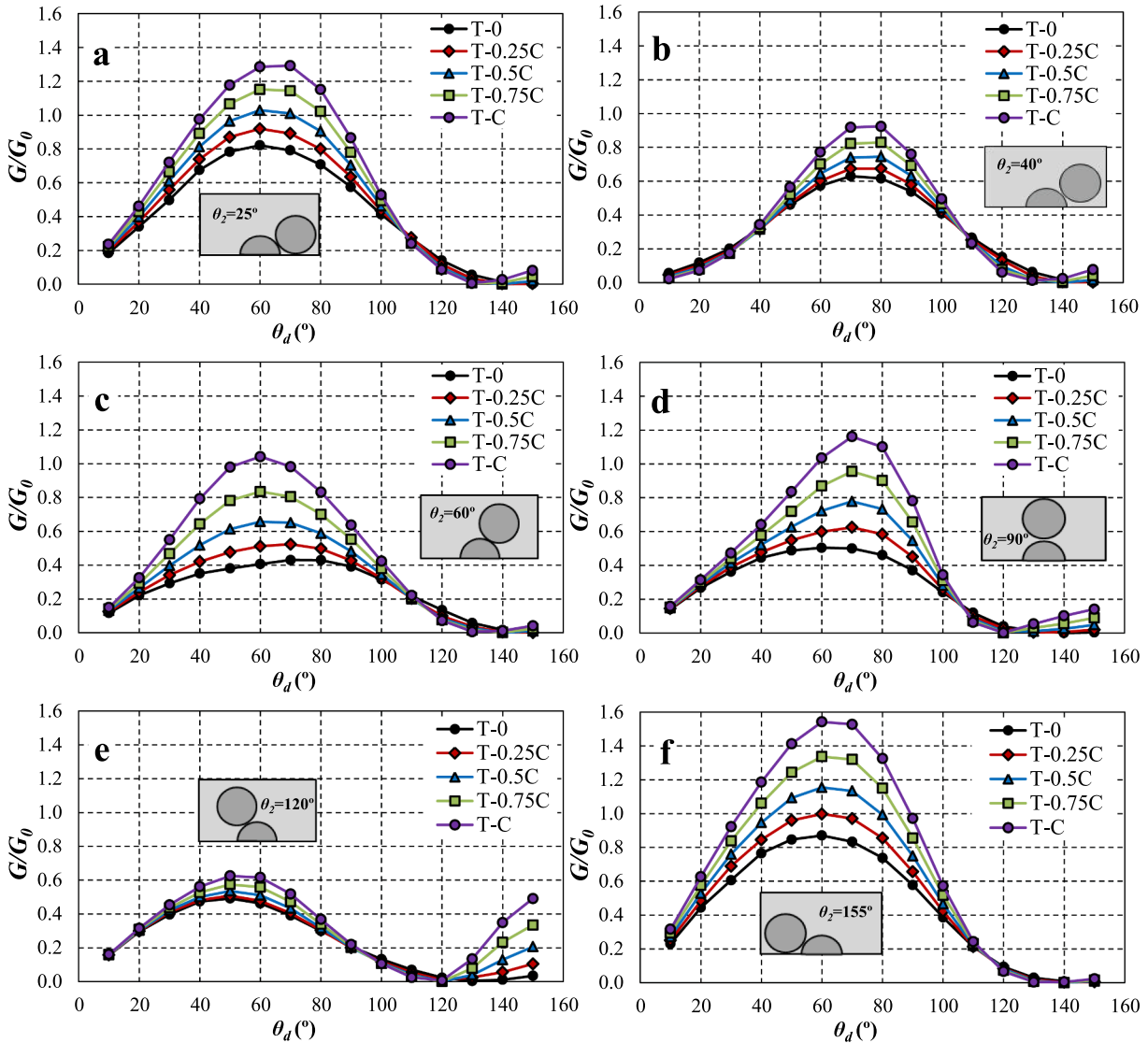

Fig. 14. G/G_0 versus θ_d for T-nC ($n = 0$, 0.25, 0.5, 0.75, 1): a) $\theta_2 = 25°$, b) $\theta_2 = 40°$, c) $\theta_2 = 60°$, d) $\theta_2 = 90°$, e) $\theta_2 = 120°$, f) $\theta_2 = 155°$.

crack growth range). For $90°\leq\theta_2\leq140°$, there is also an important increase in G evolution for $\theta_d \geq 120°$.

The comparison of these G evolutions and their corresponding single-fibre case, for each T-nC case, is plotted in Fig. 15 and Fig. 16 for $n = 0$, 0.25, 0.5, and $n = 0.5$, 0.75, 1, respectively. It is observed that, as the secondary load increases, the differences between the G evolution corresponding to every value of θ_2 and the single-fibre case also tend to

increase (as expected in view of the results of the T-nT cases), especially within the debonding range $0°\leq\theta_d\leq120°$. For T-C, these differences become very relevant for $\theta_2=120°$, the evolution of G not being very altered by the secondary load and staying considerably below the single-fibre case; on the contrary, for $\theta_2=155°$, the evolution of G is more affected by the secondary load that the single-fibre case and stays above its values of G.
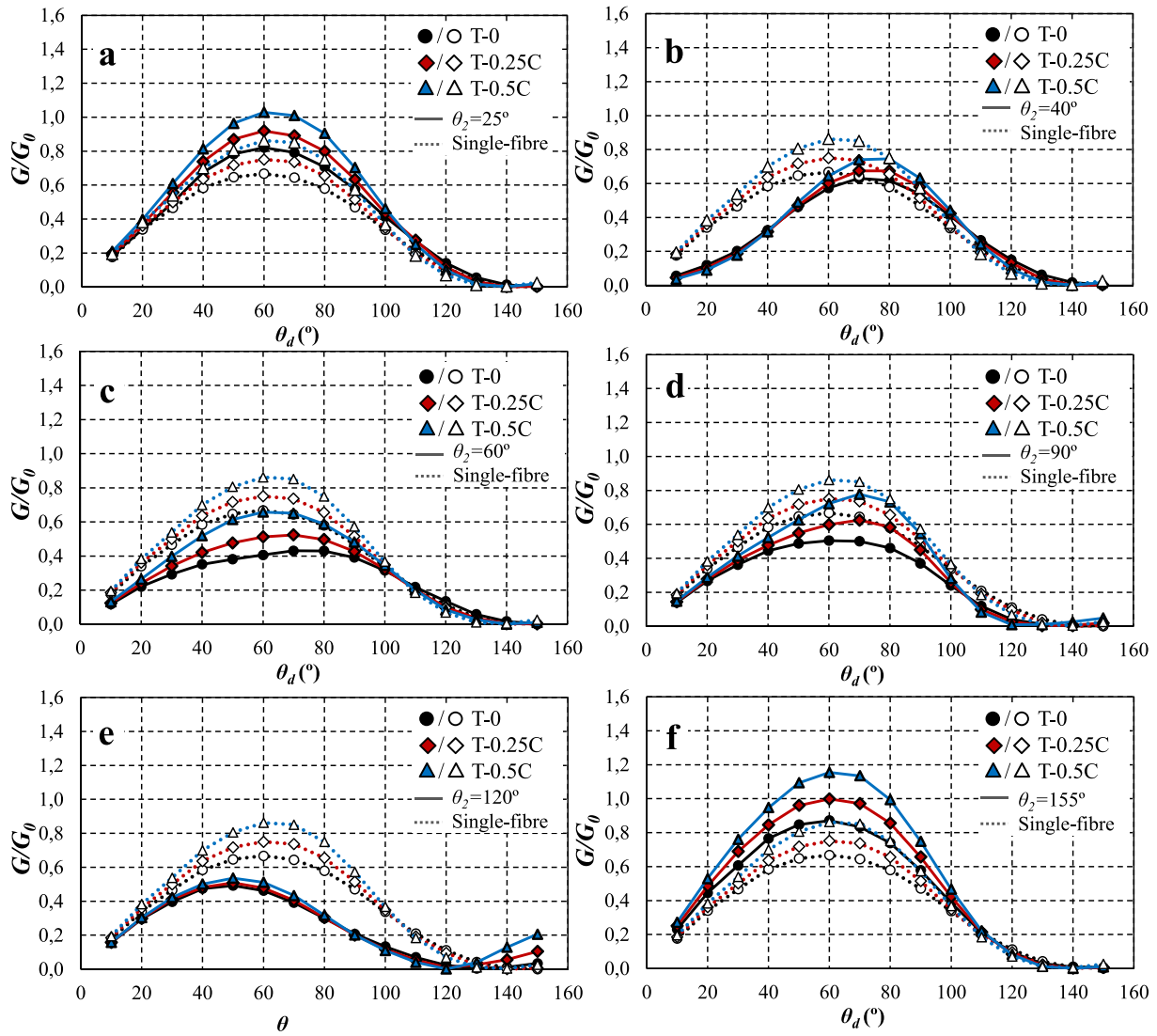
Fig. 15. Comparison of G/G_O versus θ_d for T-nC ($n = 0, 0.25, 0.5$), with reference to the single-fibre model: a) $\theta_2 = 25°$, b) $\theta_2 = 40°$, c) $\theta_2 = 60°$, d) $\theta_2 = 90°$, e) $\theta_2 = 120°$, f) $\theta_2 = 155°$.

These differences between the two-fibre and the single-fibre cases can be analysed in more detail by plotting the G evolutions for a specific T-nC case. Thus, Figs. 17 and 18 represent, for $n=0.5$ and $n=1$ respectively, the comparison between G for a selection of θ_2 values and with respect to the corresponding single-fibre case.

If Figs. 17 and 18 are compared, and with reference to the uniaxial tensile results [6], it is observed that the differences between the evolutions of G for all the two-fibre cases tend to increase as the compressive load increases, contrary to the T-nT cases.

Regarding Mode I, it is observed that G_I evolution is considerably above that corresponding to the single-fibre case for the θ_2 values for which the fibres tend to be aligned with the tensile load ($\theta_2 = 25°$, $155°$). This effect, which was already observed in [6], is related to the amplification of the radial relative displacements between the crack lips, due to the presence of a secondary fibre (stiffer than the surrounding matrix) approximately aligned with the zone of the crack where the maximum radial displacement is expected to appear (in view of the results of the single-fibre case [1,2]). When considering a transverse compressive load, this effect is intensified as n increases, as can be deduced from the G_I evolutions represented in Figs. 17 and 18.

On the contrary, when $40°≤\theta_2≤90°$, the results presented in [6] showed that there was an important decrease in G_I when compared to the single-fibre case. This effect, especially remarkable for $40°≤\theta_2≤60°$,

is also intensified by the transverse compressive load. For instance, the decrease in G_I for $\theta_2=60°$ and T-C becomes very important and, as a consequence, the main role in the propagation of the interface crack belongs to Mode II. Moreover, for all θ_2 values, the disappearance of the mixed mode propagation is more advanced as the compressive load increases, Mode I vanishes within the debonding ranges $40°≤\theta_d≤70°$ for T-0.5C and $30°≤\theta_d≤60°$ for T-C (the extreme cases are $\theta_2 = 50°$, $60°$ and $\theta_2=25°$).

The variation of the value of the Energy Release Rate for the first debond considered ($G_{\theta_d=10°}$) is represented in Fig. 19 for the T-nC cases, with respect to the single-fibre case under uniaxial tension. It can be deduced that the compressive load promotes the effects found in [6], with some differences between the θ_2 ranges. The θ_2 range for which $G_{\theta_d=10°}$ stays below the reference case, which represents a protecting effect against failure, is reduced from $30°≤\theta_2≤130°$ (T-0) to $30°≤\theta_2≤60°$ and $90°≤\theta_2≤120°$ (T-C). For T-C, this effect is intensified for $30°≤\theta_2≤40°$ and reduced for $\theta_2 = 60°$, $90°$, $130°$. For $\theta_2=50°$ and $100°≤\theta_2≤120°$, $G_{\theta_d=10°}$ is not affected. With regard to the cases for which $G_{\theta_d=10°}$ stays above the reference case (accelerative effect against failure), they correspond to $130°≤\theta_2≤155°$ and $\theta_2=25°$ for T-0, whereas for T-C, the range $70°≤\theta_2≤80°$ is also included. This accelerative effect is intensified as the compressive load increases.

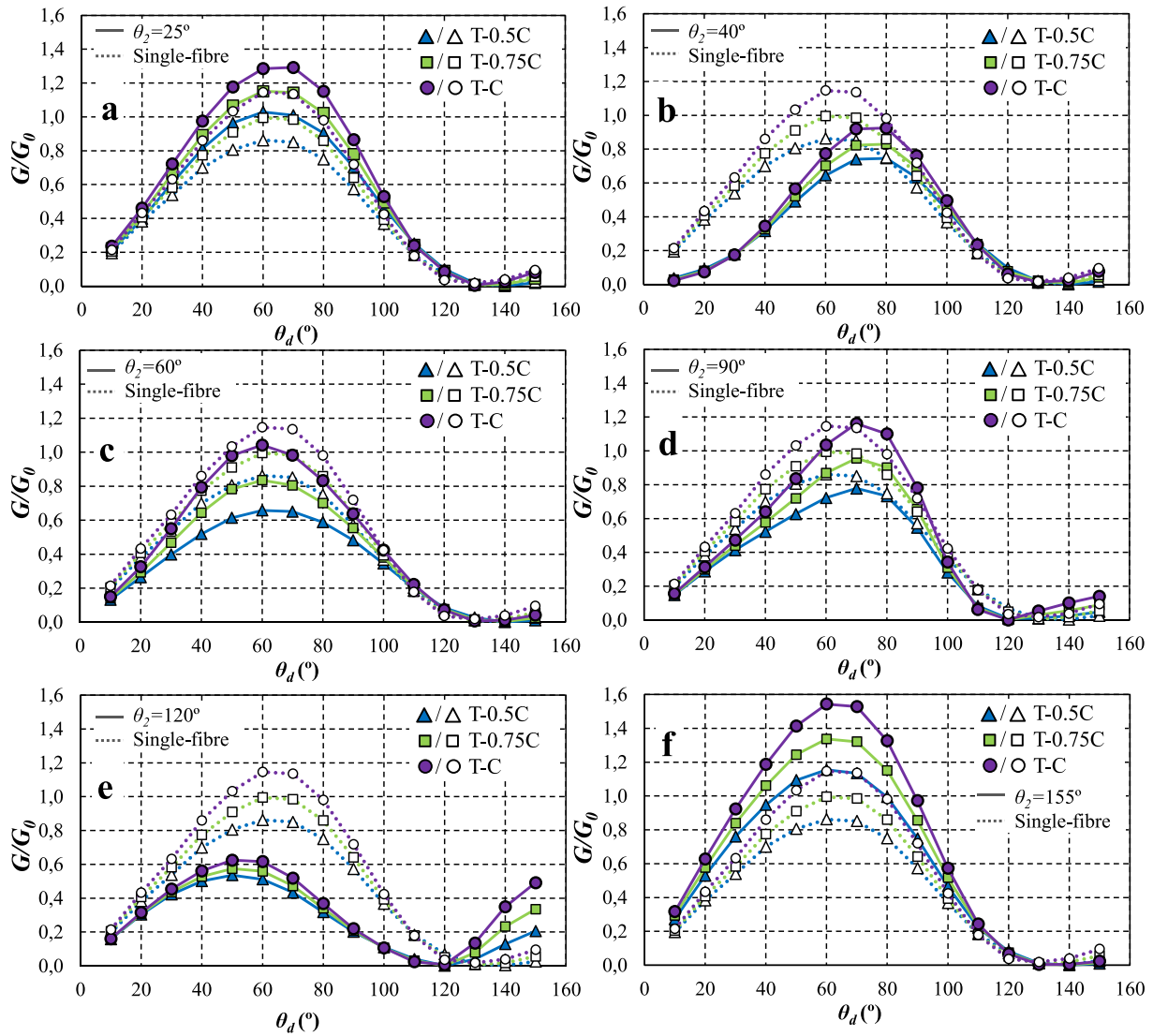**Fig. 16.** Comparison of G/G_0 versus θ_d for T-nC (n = 0.5, 0.75, 1), with reference to the single-fibre model: a) $\theta_2 = 25°$, b) $\theta_2 = 40°$, c) $\theta_2 = 60°$, d) $\theta_2 = 90°$, e) $\theta_2 = 120°$, f) $\theta_2 = 155°$.

In general, if the two-fibre cases are compared with their corresponding single-fibre case for each value of n, it can be deduced once again that, the secondary compressive load promotes the differences between all the cases, which means that the influence of the secondary fibre on the initiation of the propagation is enhanced by the compressive load.

Regarding the G value associated with the first debond considered ($G_{\theta_d=10°}$), used as a representative parameter for the evaluation of the effect of the biaxial load on the initiation of the propagation, the ratio $\sqrt{\frac{G_{\theta_d}(\text{T}-0)}{G_{\theta_d}(\text{T}-n\text{C})}}$ was calculated for all T-nC cases and the single-fibre model. The results, represented in Table 3 matches the values obtained in [31]. As could be expected in view of the values presented in Table 2 for the T-nT cases, the compressive character of the secondary load implies an accelerative effect against failure, as $\sqrt{\frac{G_{\theta_d}(\text{T}-0)}{G_{\theta_d}(\text{T}-n\text{C})}} < 1$, which means that the level of load necessary for the initiation of the propagation of the crack is lower than the one associated with the uniaxial tensile case.

With respect to the two-fibre model cases, in order to quantify the load level necessary to initiate crack propagation with respect to the single-fibre uniaxial case, the ratio $\sqrt{\frac{G_{\theta_d=10°}(\text{T}-0,\ \text{SF})}{G_{\theta_d=10°}(\text{T}-n\text{C})}}$ was also calculated

and represented in Table 3 for all θ_2 and T-nC cases. As commented before, as n increases, the differences between all θ_2 tend to increase.

4.2. Propagation of the interface crack

As previously commented in Section 3.2, the comparison between the evolution of the Energy Release Rate G, and its critical value G_c, obtained following Eq. (3), allows the end of the unstable growth to be determined. This comparison is plotted in Fig. 20 for the single-fibre case and T-nC (with n = 0, 0.25, 0.5) using the same approach presented in Section 3.2. The results agree with those presented in [31], revealing that the presence of a secondary transverse load produces shorter ranges of unstable growth than the uniaxial tension case. For the case T-0, the end of the unstable growth is predicted for a debonding angle $\theta_d \approx 55°$, whereas for T-0.5C the end of the unstable growth is obtained for $\theta_d \approx 45°$.

This comparison between G and G_c for determining the end of the unstable growth was also applied to the two-fibre cases for T-nC. To sum up, Fig. 21 represents a selection of schemes representing the lengths of unstable growth for the single-fibre and the two-fibre cases. The increase in the compressive load affects differently the two-fibre cases shown in Fig. 21. The cases $\theta_2 = 25°$, $80°$, $120°$ follow the same tendency that the

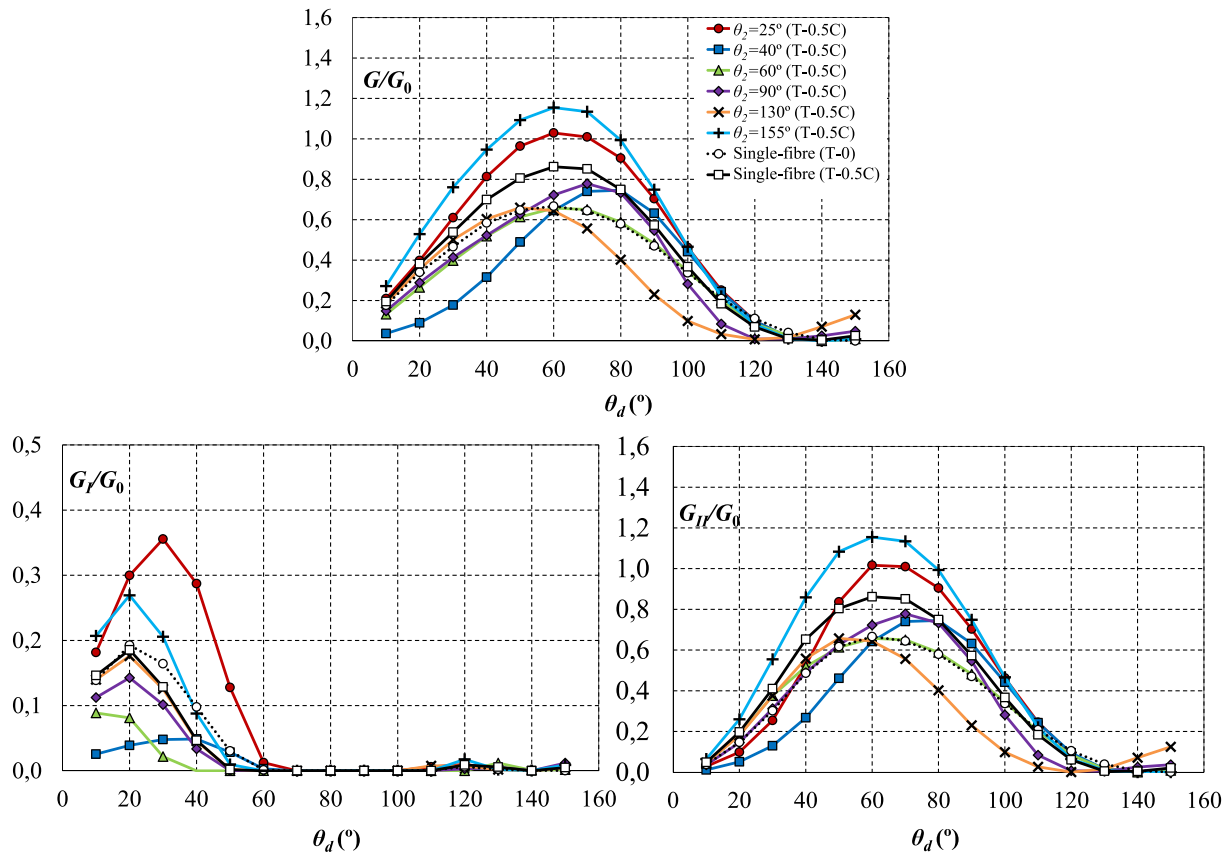**Fig. 17.** G/G_0, G_I/G_0 and G_{II}/G_0 versus θ_d for T-0.5C and $\theta_2 = 25°$, $40°$, $60°$, $90°$, $130°$, $155°$.

single-fibre case: the length of the crack being slightly shorter than the uniaxial tensile case, as the secondary load increases. However, within the range $40°{\leq}\theta_2{\leq}60°$, this reduction of the length of unstable growth becomes very significant with respect to the rest of the two-fibre cases and the single-fibre case. This effect is especially remarkable for $\theta_2{=}40°$, as the crack length decreases from $\theta_d{=}110°$ for T-0.5C, to $\theta_d{=}10°$ for T-0.75C and T-C. This situation is due to the decrease in Mode I found within the range $40°{\leq}\theta_2{\leq}60°$ since the very beginning of the propagation. Therefore, the value of the local phase angle ψ_k, which is related to the mode mixity, is much higher than those obtained for other θ_2 cases, hindering crack growth as $G_c{>}G$ for the first debond considered.

To sum up, it is important to remark that the effects of the secondary fibre on the interface crack growth present two different configurations that depend on the level of the secondary load. For the cases $n{\leq}0.5$, the influence of the secondary fibre on the crack growth is similar to the uniaxial case: for $25°{\leq}\theta_2{\leq}40°$ the interface crack reaches greater lengths of unstable growth when compared to the single-fibre case; for $\theta_2{>}40°$, the crack reaches slightly shorter or similar lengths of unstable growth than the single-fibre case. However, when $n{>}0.5$, for $25°{\leq}\theta_2{\leq}30°$ the end of the unstable growth is found for greater lengths of unstable growth than in the single-fibre case whereas for $40°{\leq}\theta_2{\leq}70°$, no unstable growth is detected. For $\theta_2{>}70°$, the end of unstable growth is achieved at values close to those found in the single-fibre case.

5. Discussion

After the description of the model implemented for the study of the interface crack growth and the results obtained for different biaxial loading configurations, in this section, the most important results are summarised and discussed. To this aim, these results are plotted, providing a 3D visualisation which shows an overview of the combination of different biaxial loadings and relative positions between the fibres, reinforcing the comprehension of the different effects found in this study.

The first result analysed is $G_{0_d=10°}/G_0$, the dimensionless value of the energy release rate for the first debond considered. As mentioned in previous sections, this value can be considered as an indicator of the inhibition or promotion that the presence of the secondary fibre involves for each biaxial configuration. In Fig. 22, this value is plotted, as a function of θ_2 and T-nC or T-nT ($n = 0, 0.25, 0.5, 0.75, 1$). The values are represented as a surface, allowing a better interpretation of the results. The grey plane represents the reference value, $G_{0_d=10°}/G_0$ for the uniaxial single-fibre case (i.e., SF / T-0). Thus, when the surface remains above the grey plane, the combination of the presence of the secondary fibre and a given biaxial configuration involves an accelerative effect on the initiation of crack growth. The protective effect appears when the surface is below the grey plane.

Moreover, as can be observed, increasing values of the secondary compressive load (T-nC cases) tends to intensify the effects found for the uniaxial case [6], both the inhibition and the promotion of the failure. The extension of the ranges where the accelerative effect was found for the uniaxial case by the presence of the second fibre ($\theta_2{=}25°$ and $130°{\leq}\theta_2{\leq}155°$), is barely affected as the secondary compressive load increases. There is only a new range of accelerative effect that emerges at $70°{\leq}\theta_2{\leq}80°$ for the biaxial configuration T-C. The configuration that most promotes the initiation of the propagation is found for $\theta_2{=}155°$ and T-C. Regarding the most protective effect of the secondary fibre against failure, it is obtained for $\theta_2{=}40°$ and T-C.

When the secondary tensile load is considered (T-nT), all the effects observed for T-nC are reversed. As the value of the secondary tensile load increases, the ranges for which the accelerative effect on the crack propagation was found tend to disappear. For T-T, any position of the secondary fibre has a protective effect against the initiation of the
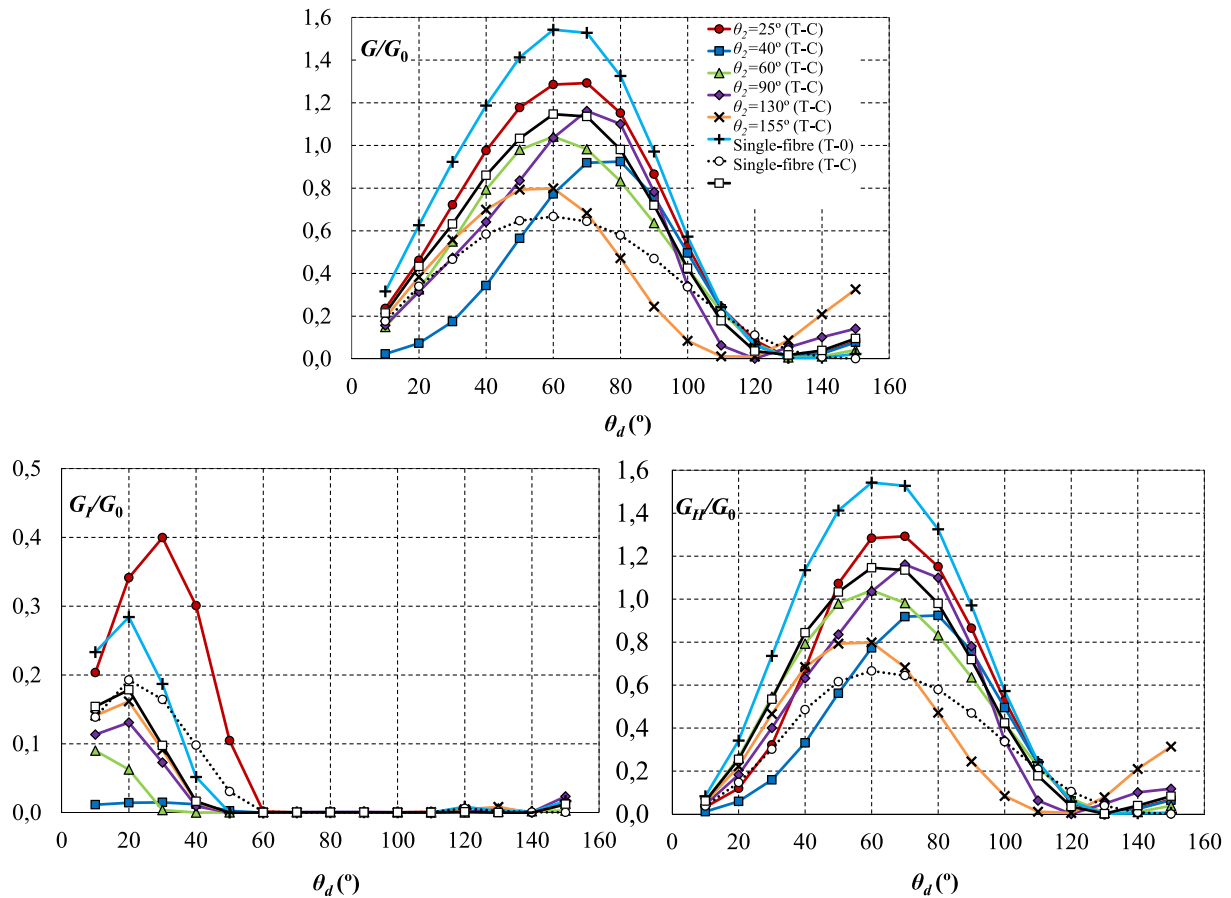
Fig. 18. G/G_0, G_I/G_0 and G_{II}/G_0 versus θ_d for T-C and $\theta_2 = 25°$, $40°$, $60°$, $90°$, $130°$, $155°$.

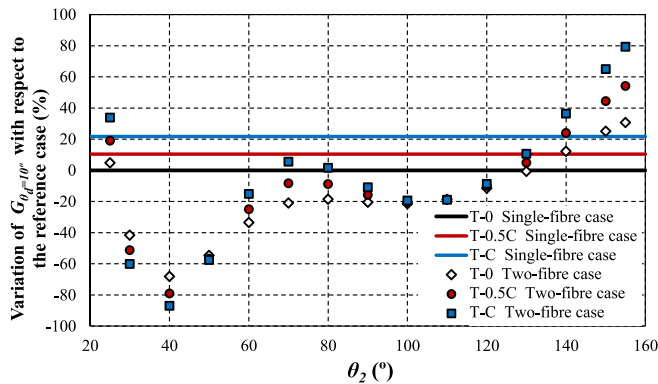**Fig. 19.** Variation of $G_{\theta_d=10°}$ for the two-fibre cases with respect to the single-fibre case (T-nC, $n = 0$, 0.5, 1).

Table 3

$\sqrt{\dfrac{G_{\theta_d=10°}\,(\mathrm{T}-0,\ \mathrm{SF})}{G_{\theta_d=10°}\,(\mathrm{T}-n\mathrm{C})}}$ for the T-nC cases and the single-fibre (SF) and two-fibre (TF) models.

Case	SF	TF $\theta_2 = 25°$	TF $\theta_2 = 30°$	TF $\theta_2 = 40°$
T-0	1.000	0.975	1.307	1.770
T-0.25C	0.975	0.945	1.365	1.958
T-0.5C	0.950	0.915	1.431	2.187
T-0.75C	0.929	0.888	1.505	2.455
T-C	0.905	0.864	1.583	2.772

Case	TF $\theta_2 = 50°$	TF $\theta_2 = 60°$	TF $\theta_2 = 70°$	TF $\theta_2 = 80°$
T-0	1.483	1.226	1.125	1.106
T-0.25C	1.502	1.187	1.083	1.076
T-0.5C	1.519	1.155	1.042	1.046
T-0.75C	1.533	1.117	1.009	1.017
T-C	1.535	1.083	0.973	0.992

Case	TF $\theta_2 = 90°$	TF $\theta_2 = 100°$	TF $\theta_2 = 110°$	TF $\theta_2 = 120°$
T-0	1.121	1.127	1.108	1.062
T-0.25C	1.106	1.123	1.107	1.057
T-0.5C	1.087	1.120	1.109	1.054
T-0.75C	1.076	1.118	1.111	1.050
T-C	1.059	1.113	1.110	1.046

Case	TF $\theta_2 = 130°$	TF $\theta_2 = 140°$	TF $\theta_2 = 150°$	TF $\theta_2 = 155°$
T-0	1.003	0.943	0.892	0.875
T-0.25C	0.989	0.920	0.860	0.837
T-0.5C	0.975	0.896	0.831	0.804
T-0.75C	0.965	0.877	0.804	0.774
T-C	0.950	0.856	0.778	0.746

propagation. Moreover, the differences between all the θ_2 cases for a given T-nT configuration are less pronounced as the value of the secondary load increases.

Another interesting analysis can be carried out if G_{max} is now plotted versus θ_2 and all the biaxial configurations. These results are plotted in Fig. 23. As can be observed for the T-nC cases, as the secondary load increases, the value G_{max} also increases. This effect is more pronounced for the ranges $25°\leq\theta_2\leq30°$, $70°\leq\theta_2\leq90°$ and $150°\leq\theta_2\leq155°$, i.e., when the relative position of the fibre tends to be aligned with the direction of the main and the secondary loads. Thus, using G_{max} as an alternative indicator of failure, and taking the T-0 case as a reference, the most accelerative effect is found for $\theta_2=155°$ and T-C, the same configuration that using $G_{\theta_d=10°}/G_0$.
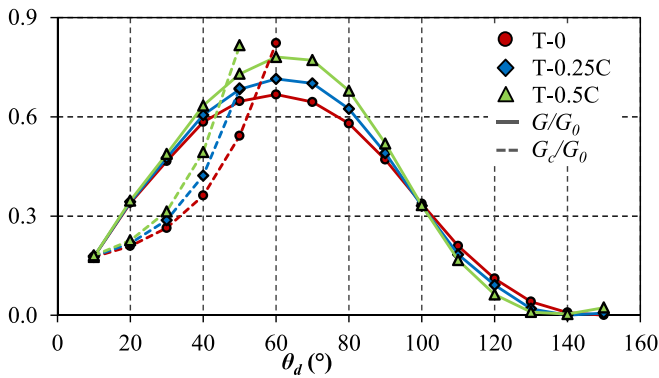
Fig. 20. G/G_0 and G_c/G_0 versus θ_d for the single-fibre case and T-nC ($n = 0$, 0.25, 0.5).

Fig. 21. Scheme of the crack length at the end of the unstable growth (T-nC).

failure being found for $\theta_2 = 70°$ and T-0.5 T. For $n > 0.5$, G_{max} tends to increase, the protective effect being maintained for all the θ_2 values, except for the range $60° \leq \theta_2 \leq 90°$ and T-T. For these cases, there is a slight accelerative effect.

Referring to all biaxial cases and as mentioned before for the analysis of $G_{\theta_d=10°}/G_0$, increasing values of the secondary compressive load intensify the differences between all θ_2 cases and as the secondary tensile load increases, these differences are attenuated. This once again reinforces the idea that T-nC cases amplify the effects caused by surrounding fibres, whereas T-nT cases reduce these effects.

The same approach presented for $G_{\theta_d=10°}/G_0$ and G_{max} can be also implemented for the final length of unstable growth obtained, θ_d^{end}, for all the relative positions between the fibres and all the biaxial configurations (Fig. 24). As commented in previous Sections and, as expected from the results presented in [31] for a single-fibre model, the crack length corresponding to the end of the unstable growth increases with the value of n for T-nT cases. However, the differences between all the θ_2 cases tend to decrease as n increases. This fact supports the idea previously commented on the attenuation of the effects of the secondary fibre caused by a secondary tensile load. The greatest lengths of unstable growth are found for $90° \leq \theta_2 \leq 100°$ and T-T ($\theta_d^{end} \approx 140°$). The greatest increase in the crack length produced by the increase of the secondary tensile load is produced for the range $60° \leq \theta_2 \leq 100°$, whereas the weakest increase is found for $25° \leq \theta_2 \leq 50°$. When a secondary compressive load is considered (T-nC), as its value increases, θ_d^{end} decreases. This fact is especially relevant for the range $40° \leq \theta_2 \leq 70°$, θ_d^{end} decreasing considerably. For this range and $n \geq 0.75$, crack growth does not occur.

These predictions about the end of the unstable growth cannot be easily confirmed by experimental approaches. The fibre distribution of a lamina does not usually correspond to the present two-fibre model, the number of neighbouring fibres being greater. Nevertheless, based on [2,29], microscopical observations of several ruptured carbon-epoxy cruciform specimens subjected to different biaxial loading have been carried out. Some quasi-isolated three-fibre clusters with the presence of an interface crack have been found, which approximately correspond to the symmetrical two-fibre model configuration. Several examples are shown in Fig. 25 where the length of the debonds has been measured. Fig. 25a corresponds to the T-0.7C loading case and Fig. 25b corresponds to the T-0 case.

In Fig. 25a and 25b, an interface crack is observed in the presence of two nearby fibres, in a quasi-symmetrical configuration. The presence of the other surrounding fibres is not negligible, as the distance from the interface crack to the fibres has to be considerably increased to avoid their effects [6,7]. Nevertheless, their influence is considerably less important than the presence of the two nearest fibres. If the relative position of these two nearby fibres with respect to the damaged fibre is analysed, it corresponds to high values of θ_2 ($\theta_2 = 143°$, 158° for Fig. 25a
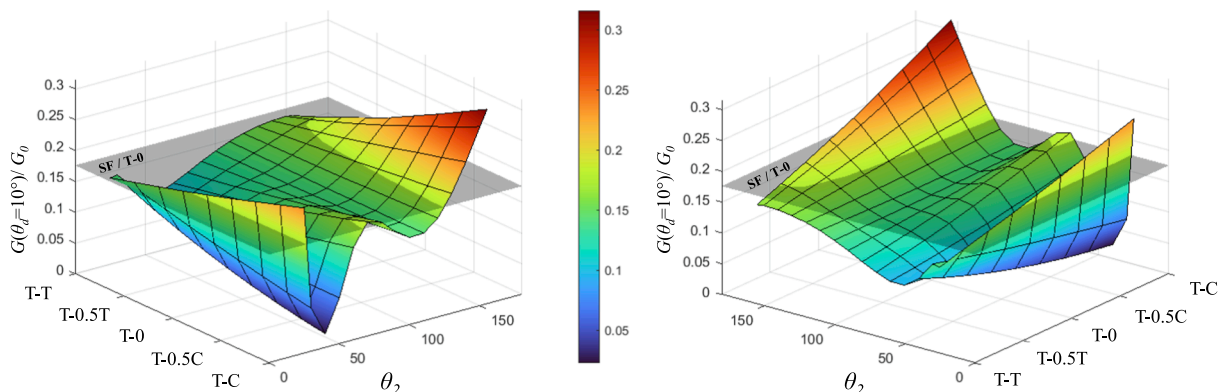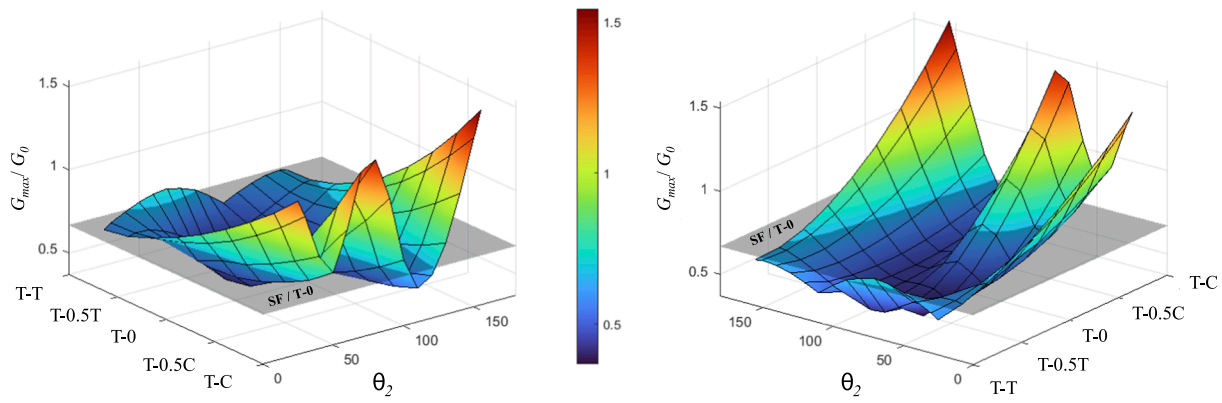
When observing the T-nT cases, as the value of the secondary load increases, the accelerative effect (which was only found within the ranges $70° \leq \theta_2 \leq 90°$ and $140° \leq \theta_2 \leq 155°$ for T-0), tends to disappear. For $n \leq 0.5$, the values of G_{max} decrease, the most protective effect against

Fig. 22. $G_{\theta_d=10°}/G_0$ versus θ_2 and all the biaxial configurations.

Fig. 23. G_{max} versus θ_2 and all the biaxial configurations.
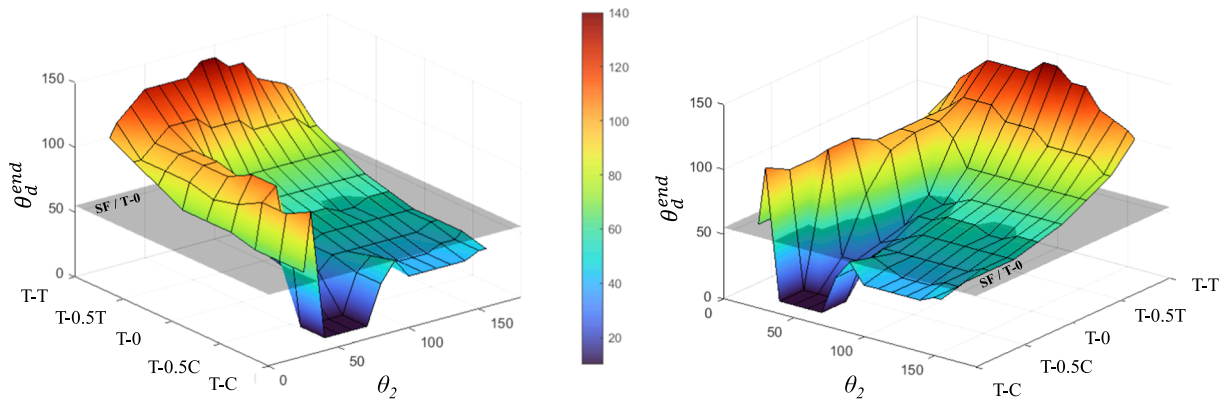

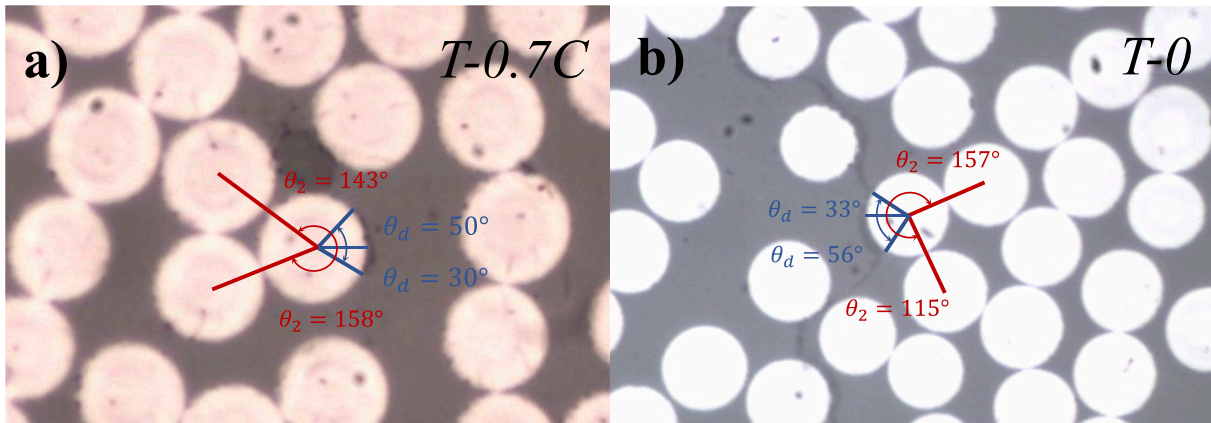**Fig. 24.** θ_d^{end} versus θ_2 and all the biaxial configurations.

Fig. 25. Microscopical observations of interface cracks at cruciform specimens subjected to biaxial loading a) T-0.7C and b) T-0.

and $\theta_2 = 115°$, $157°$ for Fig. 25b). The configuration presented in Fig. 25a could be compared with the prediction of the two-fibre model for the end of the unstable growth for the case T-0.75C. This prediction gives the values $\theta_d^{end}(\theta_2 = 155°) \approx 50°$ and $\theta_d^{end}(\theta_2 = 140°) \approx 45°$, which corresponds to a total crack length of 95°. This prediction is relatively close to the microscopical observation (total crack length of 80°). The difference in the crack length and its lack of symmetry could be associated with the influence of the rest of the fibres and the slight difference between both loading cases. For the uniaxial case represented in Fig. 25b, the prediction of the two-fibre model gives $\theta_d^{end}(\theta_2 = 155°) \approx 50°$ and $\theta_d^{end}(\theta_2 = 110°, 120°) \approx 40°$, and a total length of 90°, in full agreement with the total length of the microscopical observation (89°).

Considering all the information provided by Figs. 22-24, the influence of the secondary fibre is more important for the T-nC cases and increasing values of n. This fact would imply that, experimentally, if each biaxial configuration is applied progressively, and observing for a similar applied load, interface cracks should appear before and they could be more frequently observed for T-nC and the range $150° \leq \theta_2 \leq 155°$, even though the crack lengths would be considerably shorter than in the uniaxial case. Interface cracks should be rarely observed also for $\theta_2 = 40°$ and T-C. In general, and for the same applied load, for T-nT and increasing values of n, interface cracks observation should be less frequent than for T-nC, even though the extent of cracks

should be greater. These predictions cannot be easily checked in terms of the comparison between the T-nT and the T-nC cases, as the experimental results reveal that the external load at the moment of rupture is lower for the T-nC cases, and the failure is very explosive [35]. However, this fact agrees with the increase in the accelerative effects found for the T-nC cases and the generalised protective effect of the T-nT cases.

6. Conclusions

In this work, the propagation of an interface crack subjected to biaxial loading has been studied by means of a two-fibre BEM model. The objective was to analyse the effect of the presence of a nearby fibre on the interface crack growth under different loading configurations. The biaxial configuration consists in a main tensile load, nominally responsible for the failure and a secondary tensile or compressive load, perpendicular to the main load.

The results have been analysed under the light of Interfacial Fracture Mechanics. Thus, this work has been focused on the study of the Energy Release Rate for different configurations of the two-fibre model, in order to compare the results with previous uniaxial and biaxial single-fibre studies. This comparison is based on the influence of three main parameters: the type of secondary load (tensile or compressive), the level of load and the relative position between the fibres. Some of the most important conclusions are summarised next.

With regard to the effects of the biaxial loading and the secondary fibre on the propagation of the interface crack, some effects were observed as the secondary load increased:

- With reference to the uniaxial case, when considering a secondary tensile load and its value increased, the end of the unstable growth was produced at greater debonding angles for a fixed value of θ_2. Nevertheless, a secondary compressive load implied, for most of the cases, shorter crack lengths at the end of the unstable growth. These effects were already detected for a single-fibre model in [31], but the intensity of the effects depends on the position of the secondary fibre.
- For the T-nT biaxial configuration, as the secondary load increased the differences between the θ_2 cases and their corresponding single-fibre case became smaller. On the contrary, for the T-nC cases, these differences were more accentuated as the secondary load increased.
- For increasing values of the transverse tensile load, the θ_2 ranges for which the length of unstable growth was greater than its corresponding single-fibre case were wider. However, as the secondary compressive load increased, this fact only occurred for a few relative positions between the fibres.

Additionally, micromechanical experimental evidence has been presented supporting the aforementioned conclusions.

According to the study of the Energy Release Rate for a given biaxial configuration and a relative position between the fibres, the maximum and initial values (G_{max} and $G_{\theta_d=10°}$) were used as representative parameters of the inhibitions or promotion of failure, with respect to the uniaxial single-fibre case. In this regard, when a secondary tensile load was included (T-nT), for most of the relative positions between the fibres the presence of the nearby fibre intensified the inhibition and reduced the promotion of the mechanism of failure observed in the uniaxial tensile case [6]. For T-nC, the biaxial loads implied the opposite effect, intensifying the most protective or accelerative effects found in [6].

On a final note, considering the combination of both effects, biaxial loading and the surrounding fibre, on the aspects analysed in this study (with reference to the uniaxial single-fibre case), as the level of the secondary tensile load increases, the biaxial loading tends to inhibit the presence of the undamaged secondary fibre. On the contrary, when a secondary compressive load is considered, as its value increases, all the alterations induced by the secondary fibre are intensified.

CRediT authorship contribution statement

Carlos Sandino: Methodology, Validation, Investigation, Writing – review & editing. **Elena Correa:** Conceptualization, Methodology, Validation, Writing – review & editing, Supervision, Funding acquisition. **Federico París:** Conceptualization, Writing – review & editing, Supervision, Funding acquisition.

Declaration of Competing Interest

The authors declare that they have no known competing financial interests or personal relationships that could have appeared to influence the work reported in this paper.

Data availability

Data will be made available on request.

References

[1] F. París, E. Correa, J. Cañas, Micromechanical view of failure of the matrix in fibrous composite materials, Compos. Sci. Technol. 63 (7) (2003) 1041–1052.

[2] F. París, E. Correa, V. Mantič, Kinking of transversal interface cracks between fibre and matrix, J. App. Mech. 74 (4) (2007) 703–716.

[3] E. Correa, V. Mantič, F. París, Numerical characterisation of the fibre-matrix interface crack growth in composites under transverse compression, Eng. Fract. Mech 75 (14) (2008) 4085–4103.

[4] E. Correa, V. Mantič, F. París, A micromechanical view of inter-fibre failure of composite materials under compression transverse to the fibres, Compos. Sci. Technol. 68 (9) (2008) 2010–2021.

[5] E. Correa, F. París, V. Mantič, Effect of thermal residual stresses on the matrix failure under transverse compression at micromechanical level – a numerical and experimental study, Compos. Part A- Appl. S 43 (1) (2012) 87–94.

[6] C. Sandino, E. Correa, F. París, Numerical analysis of the influence of a nearby fibre on the interface crack growth in composites under transverse tensile load, Eng. Fract. Mech 168 (2016) 58–75.

[7] C. Sandino, E. Correa, F. París, A study of the influence of a nearby fibre on the interphase crack growth under transverse compression in composite materials, Eng. Fract. Mech. 193 (2018) 1–16.

[8] V.I. Kushch, S.V. Shmegera, P. Brøndsted, L. Mishnaevsky, Numerical simulation of progressive debonding in fiber reinforced composite under transverse loading, Int. J. Engng. Sci. 49 (1) (2011) 17–29.

[9] L. Távara, V. Mantič, E. Graciani, F. París, Modelling interfacial debonds in unidirectional fibre-reinforced composites under biaxial transverse loads, Compos. Struct. 136 (2016) 305–312.

[10] V. Mantič, Interface crack onset at a circular cylindrical inclusion under a remote transverse tension. application of a coupled stress and energy Criterion, Int. J. Solids Struct. 46 (6) (2009) 1287–1304.

[11] P.A. Carraro, M. Quaresimin, Modelling fibre–matrix debonding under biaxial loading, Compos. A Appl. Sci. Manuf. 61 (2014) 33–42.

[12] M. Hojo, M. Mizuno, T. Hobbiebrunken, T. Adachi, M. Tanaka, S.K. Ha, Effect of fiber array irregularities on microscopic interfacial normal stress states of transversely loaded UD-CFRP from viewpoint of failure initiation, Compos. Sci. Technol. 69 (11–12) (2009) 1726–1734.

[13] F. Sharifpour, J. Montesano, R. Talreja, Assessing the effects of ply constraints on local stress states in cross-ply laminates containing manufacturing induced defects, Compos. B Eng. 199 (2020).

[14] L. Zhuang, R. Talreja, J. Varna, Transverse crack formation in unidirectional composites by linking of fibre/matrix debond cracks, Compos. A 107 (2018) 294–303.

[15] L. Zhuang, A. Pupurs, J. Varna, R. Talreja, Z. Ayadi, Effects of inter-fiber spacing on fiber-matrix debond crack growth in unidirectional composites under transverse loading, Compos. A 109 (2018) 463–471.

[16] L. Di Stasio, J. Varna, Z. Ayadi, Energy release rate of the fiber/matrix interface crack in UD composites under transverse loading: effect of the fiber volume fraction and of the distance to the free surface and to non-adjacent debonds, Theor. Appl. Fract. Mech. 103 (2019) 102251.

[17] L. Di Stasio, J. Varna, Z. Ayadi, Effect of the proximity to the 0°/90° interface on Energy Release Rate of fiber/matrix interface crack growth in the 90°-ply of a cross-ply laminate under tensile loading, J. Compos. Mater. 54 (21) (2020) 3021–3034.

[18] H. Saito, H. Takeuchi, I. Kimpara, A study of crack suppression mechanism of thin-ply carbon-fiber-reinforced polymer laminate with mesoscopic numerical simulation, J. Compos. Mater. 48 (17) (2014) 2085–2096.

[19] Arteiro A, Catalanotti G, Melro AR, Linde P, Camanho PP. Micro-mechanical analysis of the effect of ply thickness on the transverse compressive strength of polymer composites. Compos Part A-Appl Sci Manuf 2015; 79: 127–37.

[20] París F, Velasco ML, Correa E. The scale effect in composites: An explanation physically based on the different mechanisms of damage involved in failure. Compos Struct 2021;257:113089.

[21] H. Zhang, M.L. Ericson, J. Varna, L.A. Berglund, Transverse single-fibre test for interfacial debonding in composites: 1. experimental observation, Compos. Part A-Appl. Sci. Manuf. 28 (4) (1997) 309–315.

[22] E.K. Gamstedt, B. Sjögren, Micromechanics in tension-compression fatigue of composite plies containing transverse plies, Compos. Sci. Technol. 59 (1999) 167–178.

[23] M. Gentz, D. Armentrout, P. Rupnowski, L. Kumosa, E. Shin, J.K. Sutter, M. Kumosa, In-plane shear testing of medium and high modulus woven graphite fiber reinforced/polyimide composites, Compos. Sci. Technol. 64 (2) (2004) 203–220.

[24] N. Baral, H. Guezenoc, P. Davies, C. Baley, High modulus carbon fibre composites: correlation between transverse tensile and Mode I interlaminar fracture properties, Mater. Lett. 62 (6-7) (2008) 1096–1099.

[25] T. Hobbiebrunken, M. Hojo, T. Adachi, C. De Jong, B. Fiedler, Evaluation of interfacial strength in CF/epoxies using FEM and in-situ experiments, Compos. A 37 (12) (2006) 2248–2256.

[26] H. Saito, H. Takeuchi, I. Kimpara, Experimental evaluation of the damage growth restraining in 90° layers of thin-ply CFRP cross-ply laminates, Adv. Compos. Mater 21 (1) (2012) 57–66.

[27] K. Martinyuk, B.F. Sørensen, P. Modregger, E.M. Lauridsen, 3D *in situ* observations pf glass fibre/matrix interfacial debonding, Compos. Part A- Appl. Sci. Manuf. 55 (2013) 63–73.

[28] E. Correa, M.I. Valverde, M.L. Velasco, F. París, Microscopical observations of inter-fibre failure under tension, Compos. Sci. Technol. 155 (2018) 213–220.

[29] P.L. Zumaquero, E. Correa, J. Justo, F. París, Microscopical observations of interface cracks from inter-fibre failure under compression in composites laminates, Compos Part A-Appl Sci Manuf 110 (2018) 76–83.

[30] Z. Hashin, A. Rotem, A fatigue failure criterion for fibre reinforced materials, J. Comp. Mat. 7 (1973) 448–464.

[31] E. Correa, F. París, V. Mantič, Effect of the presence of a secondary transverse load on the inter-fibre failure under tension, Eng. Fract. Mech. 103 (2013) 174–189.

[32] E. Correa, F. París, V. Mantič, Effect of a secondary transverse load on the inter-fibre failure under compression, Compos. B 65 (2014) 57–68.

[33] E. Correa, A. Barroso, M.D. Pérez, F. París, Design for a cruciform coupon used for tensile biaxial transverse test son composite materials, Compos. Sci. Technol. 145 (2017) 138–148.

[34] A. Barroso, E. Correa, J. Freire, F. París, A device for biaxial testing in uniaxial machines. design, manufacturing and experimental results using cruciform specimens of composite materials, Exp. Mech. 58 (1) (2018) 49–53.

[35] P. Lucía Zumaquero, E. Correa, J. Justo, F. París, Transverse biaxial tests on long fibre reinforced composites, Comput. Struct. 297 (2022).

[36] París F, Cañas J. Boundary element method. Fundamentals and applications. Oxford: OUP; 1997.

[37] E. Graciani, V. Mantič, F. París, A. Blázquez, Weak formulation of axi-symmetric frictionless contact problems with boundary elements, Application to interface cracks. Comput. Struct. 83 (10-11) (2005) 836–855.

[38] G.R. Irwin, Analysis of stresses and strain near the end of a crack transversing a plate, J. App. Mech. 24 (1957) 361–364.

[39] M. Toya, A crack along the interface of a circular inclusion embedded in an infinite solid, J. Mech. Phys. Solids 22 (5) (1974) 325–348.

[40] Murakami Y. Stress intensity factor handbook. Oxford: Pergamon Press; 1988.

[41] M.L. Velasco, E. Correa, F. París, Interaction between fibres in the transverse damage in composites, Eng. Fract. Mech. 239 (2020).

[42] J.W. Hutchinson, Z. Suo, Mixed mode cracking in layered materials, Adv. App. Mech. 29 (1992) 63–191.

[43] V. Mantič, F. París, Relation between SIF and ERR based measures of fracture mode mixity in interface cracks, Int. J. Fracture 130 (2) (2004) 557–569.

[44] J. Dundurs, Discussion of a paper by DB Bogy, J Appl Mech 36 (1968) 650–652.